TUDelft

Delft University of Technology

Charge carrier trapping management in Bi^{3+} and lanthanides doped Li(Sc,Lu)GeO$_4$ for x-ray imaging, anti-counterfeiting, and force recording

Lyu, Tianshuai; Dorenbos, Pieter

Important note
To cite this publication, please use the final published version (if applicable).
Please check the document version above.

Charge carrier trapping management in Bi³⁺ and lanthanides doped Li(Sc,Lu)GeO₄ for x-ray imaging, anti-counterfeiting, and force recording 🅕

Tianshuai Lyu ✉ 🆔 ; Pieter Dorenbos 🆔

Check for updates

View Online   Export Citation   CrossMark

06 March 2024 10:41:49

AIP Publishing

Charge carrier trapping management in Bi^{3+} and lanthanides doped Li(Sc,Lu)GeO$_4$ for x-ray imaging, anti-counterfeiting, and force recording

View Online   Export Citation   CrossMark

Tianshuai Lyu[1,a] (iD) and Pieter Dorenbos[2] (iD)

AFFILIATIONS

[1]Xiamen Key Laboratory of Optoelectronic Materials and Advanced Manufacturing, Institute of Luminescent Materials and Information Displays, College of Materials Science and Engineering, Huaqiao University, Xiamen 361021, China

[2]Section Luminescence Materials, Department of Radiation Science and Technology, Faculty of Applied Sciences, Delft University of Technology, Mekelweg 15, 2629JB Delft, The Netherlands
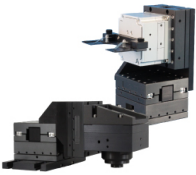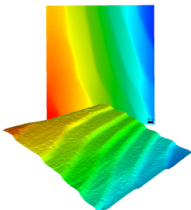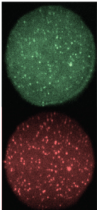
Note: This paper is part of the special collection on Energy Storage and Conversion.
[a]Author to whom correspondence should be addressed: lv_tianshuai@126.com and lv_tianshuai@hqu.edu.cn

ABSTRACT

Discovering energy storage materials with rationally controlled trapping and de-trapping of electrons and holes upon x-rays, UV-light, or mechanical force stimulation is challenging. Such materials enable promising applications in various fields, for instance in multimode anti-counterfeiting, x-ray imaging, and non-real-time force recording. In this work, photoluminescence spectroscopy, the refined chemical shift model, and thermoluminescence studies will be combined to establish the vacuum referred binding energy (VRBE) diagrams for the LiSc$_{1-x}$Lu$_x$GeO$_4$ family of compounds containing the energy level locations of Bi^{2+}, Bi^{3+}, and the lanthanides. The established VRBE diagrams are used to rationally develop Bi^{3+} and lanthanides doped LiSc$_{1-x}$Lu$_x$GeO$_4$ storage phosphors and to understand trapping and de-trapping processes of charge carriers with various physical excitation means. The thermoluminescence intensity of x-ray irradiated LiSc$_{0.25}$Lu$_{0.75}$GeO$_4$:0.001Bi^{3+},0.001Eu^{3+} is about two times higher than that of the state-of-the-art x-ray storage phosphor BaFBr(I):Eu^{2+}. Particularly, a force induced charge carrier storage phenomenon appears in Eu^{3+} co-doped LiSc$_{1-x}$Lu$_x$GeO$_4$. Proof-of-concept non-real-time force recording, anti-counterfeiting, and x-ray imaging applications will be demonstrated. This work not only deepens our understanding of the capturing and de-trapping processes of electrons and holes with various physical excitation sources, but can also trigger scientists to rationally discover new storage phosphors by exploiting the VRBEs of bismuth and lanthanide levels.

Published under an exclusive license by AIP Publishing. https://doi.org/10.1063/5.0175390

I. INTRODUCTION

A storage phosphor is known as a material which can store free electrons and holes in deep traps during exposure to ultraviolet light[1] or ionizing radiation like x-rays, β-ray, or gamma rays.[2] It has been utilized for various applications,[3] for example, in the structural inspection of curved objects like in dental imaging, dosimetry for radiation dose measurement,[4] and x-ray computed tomography (CT).[5,6] BaFBr (I):Eu^{2+} is the state-of-the-art x-ray storage phosphor.[7] However, it can absorb water from air gradually leading to loss of the charge carrier storage capacity. New alternatives with good chemical stability and high charge carrier storage capacity are then required.

Mechanoluminescence (ML) compounds are known as materials that show instantaneous light emission during mechanical force excitation.[8] They have promising utilization for various fields,[9,10] for instance, in optical sensors for human–computer interaction, wearable sport light sources, visualization of compression force distribution,[11] and structure damage inspection.[12] However, the photon emissions from ML materials are required to be constantly detected by using expensive photomultipliers or metal oxide semiconductor (CMOS) light sensors. For near-distance ML imaging, the CMOS sensor can be easily damaged when it is closely placed underneath the ML material based film.[13] Although different compounds have been explored for mechanoluminescence, ZnS:Cu$^+$,Mn^{2+} is still the state-of-the-art mechanoluminescence compound.

Recently, a non-real-time force sensing technique has become a promising alternative for stress recording. This technique is based on force induced charge carrier storage.[14] It has potential utilization in various applications, for example, in the recording of the collision trace

06 March 2024 10:41:49

in vehicle accidents where the mechanical excitation happens randomly and suddenly. Unfortunately, the force induced charge carrier storage phenomenon is rarely discussed in the literature. Few examples are Ga^{3+} or Ge^{4+} doped $LiTaO_3$:0.005Bi^{3+}, 0.006Tb^{3+} in Ref. 15, and Eu^{2+} or Yb^{2+} doped $BaSi_2O_2N_2$:Dy^{3+} in Ref. 16. Part of their thermoluminescence (TL) glow curves are close to room temperature (RT), which means that stored information will slowly fade. Therefore, there is great interest to discover new materials where force induced charge carrier can be stored in deep traps.

The capturing and release processes of free charge carriers are of interest to unravel the mechanism of storage phosphors and to rationally develop compounds with suitable charge carrier trapping depth for different applications.[17] One then requires knowledge on the energy level locations of charge carrier trapping centers with respect to that of the conduction band (CB) bottom and the valence band (VB) top.[18] It is not until 2012 that a vacuum referred binding energy (VRBE) diagram can be constructed by using the chemical shift model.[19] It enables to determine the electron binding at different lanthanide charge carrier capturing centers, CB bottom, and VB top in different compounds with respect to the same vacuum level.[20] A refinement to the chemical shift model was proposed in Ref. 21 to establish more accurate VRBE diagrams. Like lanthanides, Bi^{3+} and Bi^{2+} can also act as good charge carrier trapping centers.[22,23] However, the VRBE diagrams containing the energy levels of Bi^{3+} and Bi^{2+} are rarely reported. It is then challenging to discuss the trapping and release processes of bismuth or/and lanthanide doped compounds. For example, ultraviolet-A (UVA) persistent luminescence emerges in Bi^{3+} doped $LiScGeO_4$ irradiated by 254 nm UV-light.[24] However, the nature of trapping and de-trapping of electrons and holes is not fully clear.

In this work, photoluminescence spectroscopy, the refined chemical shift model, and thermoluminescence will be combined to establish the vacuum referred binding energy (VRBE) diagrams for the $LiScGeO_4$, $LiSc_{0.25}Lu_{0.75}GeO_4$, and $LiLuGeO_4$ family of compounds in Figs. 1, S1, and S2. The photoluminescence emission (PL) and excitation (PLE) spectra of undoped, Eu^{3+}, Bi^{3+}, Tb^{3+}, or Pr^{3+} single doped

$LiScGeO_4$ and $LiSc_{0.25}Lu_{0.75}GeO_4$ will first be studied at 10 K or RT. The results will be utilized to construct the VRBE diagrams. The VRBEs in the ground and excited states of Bi^{3+}, Bi^{2+}, trivalent, and divalent lanthanides will be discussed.

Guided by the established VRBE diagrams in Figs. 1, S1, and S2, we will demonstrate how a deeper understanding of the trapping and de-trapping processes of charge carriers with various physical excitations will be realized for the rational exploration of storage phosphors for various applications. As a demonstration, Bi^{3+} or/and Ln^{3+} (Ln = Tb, Pr, or Eu) doped $LiSc_{1-x}Lu_xGeO_4$ will be systematically studied. It will be evidenced that Eu^{3+} works as a ~1.0 eV deep electron capturing, while Bi^{3+}, Tb^{3+}, or Pr^{3+} work as about 1.5, 2, or 2 eV deep hole capturing and recombination centers in $LiScGeO_4$. The Eu^{3+} electron trapping depth can be engineered by adjusting x in $LiSc_{1-x}Lu_xGeO_4$:0.001Bi^{3+},0.001Eu^{3+} and $LiSc_{1-x}Lu_xGeO_4$: 0.005Tb^{3+}, 0.001Eu^{3+}, leading to conduction band engineering. The integrated TL intensity of the optimized $LiSc_{0.25}Lu_{0.75}GeO_4$: 0.001$Bi^{3+}$,0.001$Eu^{3+}$ irradiated by x-rays is about two times higher than that of the state-of-the-art x-ray storage phosphor BaFBr(I):Eu^{2+}. Particularly, a force induced charge carrier storage phenomenon appears in the Bi^{3+},Eu^{3+}- and Tb^{3+},Eu^{3+}-codoped $LiSc_{1-x}Lu_xGeO_4$ (x = 0–1) compounds. The effect of mechanical or optical stimulation on the capturing and release processes of charge carriers will be discussed.

Proof-of-concept non-real-time force recording, anti-counterfeiting, and x-ray imaging applications will be demonstrated by utilizing the developed $LiSc_{1-x}Lu_xGeO_4$ storage phosphors. During exposure to high energy x-ray or ultraviolet light like 254 nm, energy storage occurs by means of trapping of charge carriers. The created free electron is trapped by Eu^{3+} to form Eu^{2+}, and the free holes are captured by Bi^{3+}, Tb^{3+}, or Pr^{3+} to form Bi^{4+}, Tb^{4+}, or Pr^{4+}. De-trapping of stored electrons at Eu^{2+} and holes at Bi^{4+}, Tb^{4+}, and Pr^{4+} can be realized by an optically stimulated luminescence process with a wide range 365–850 nm light stimulation.

This work not only deepens our understanding of the capturing and de-trapping processes with various physical excitations but also

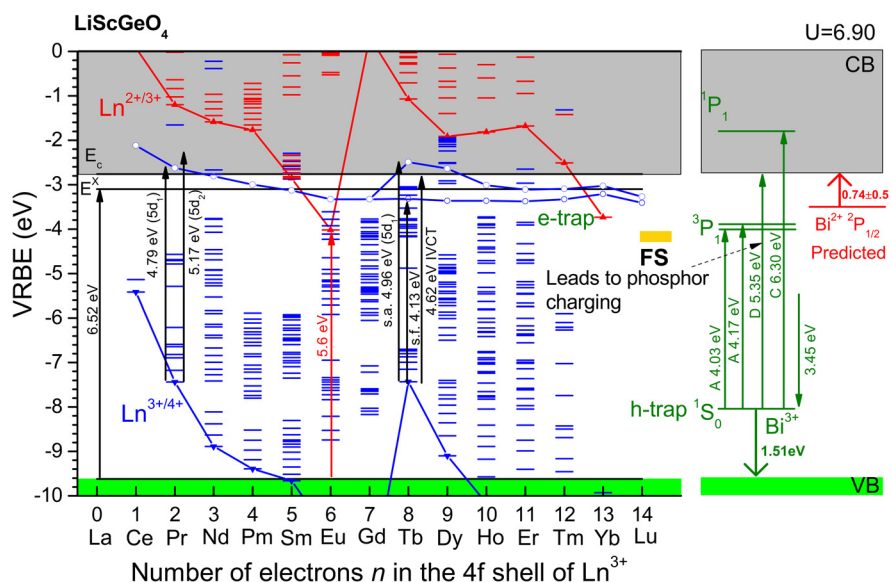**FIG. 1.** Vacuum referred binding energy (VRBE) diagram for $LiScGeO_4$ with the energy level locations of Bi^{3+}, Bi^{2+}, different divalent, and trivalent lanthanides. Experimentally observed transitions have been denoted by arrows. FS denotes traps for force induced charge carrier storage. The binding energies at the conduction band (CB) bottom and host exciton have been denoted by E_c and E_x, respectively.

develops excellent storage phosphors with high charge carrier storage capacity and good chemical stability. This work then can trigger more scientists to rationally develop new storage phosphors by constructing and using the VRBEs in bismuth and lanthanide energy level locations in different compounds.

II. RESULTS

A. Photoluminescence spectroscopy for VRBE diagram construction

To construct the vacuum-referred binding energy (VRBE) diagrams for the $LiSc_{1-x}Lu_xGeO_4$ family of compounds, the U-value (energy difference between the Eu^{2+} and Eu^{3+} ground states), energy of host exciton creation (E^{ex}), energy for charge transfer (CT) from valence band (VB) to Eu^{3+} (VB→Eu^{3+} CT), and energy for charge transfer from Bi^{3+} to conduction band are needed. The U-value can be estimated with the methods in Ref. 25 from which $U(LiScGeO_4) = 6.90$ eV and $U(LiLuGeO_4) = 6.95$ eV are estimated. Photoluminescence excitation (PLE) and emission (PL) spectra for the undoped, Bi^{3+}, or lanthanide Ln^{3+} (Ln = Eu, Pr, or Tb) single doped $LiScGeO_4$ and $LiSc_{0.25}Lu_{0.75}GeO_4$ solid solution are needed.

Figure 2(a) shows the PLE and PL spectra for the undoped $LiScGeO_4$ host at 10 K. Upon a 191 nm excitation, a broad self-trapped exciton emission band located at ~501 nm with a weak shoulder band at ~329 nm appears. Monitored at 501 nm, a strong excitation band located at ~190.5 nm emerges, which will be assigned to the $LiScGeO_4$ host exciton creation ($E^{ex} = 6.52$ eV).

Figure 2(b) shows the PLE ($\lambda_{em} = 612$ nm) and PL ($\lambda_{ex} = 223$ nm) spectra of $LiScGeO_4$:$0.01Eu^{3+}$ recorded at room temperature (RT). Upon a 223 nm excitation, line emission bands emerge in the spectral range from 550 to 700 nm because of the typical $^5D_0 \rightarrow {}^7F_j$ (j = 0–4) transitions of Eu^{3+}. Monitored at 612 nm, the excitation spectrum is composed of an excitation band peaked at ~223 nm and several line excitation bands in the spectral range from ~280 to ~400 nm, which are assigned to characteristic Eu^{3+} 4f → 4f transitions. The 223 nm excitation band will be associated with the charge transfer (CT) from the valence band (VB) to Eu^{3+}, i.e., $O^{2-} \rightarrow Eu^{3+}$ CT.[26] Fig. 2(c) further shows the PLE ($\lambda_{em} = 612.2$ nm) and PL ($\lambda_{ex} = 217$ nm) spectra of $LiScGeO_4$:$0.005Eu^{3+}$ recorded in the spectral range from 125 to 700 nm at 10 K. An excitation band peaked near 217 nm is observed. We have used 5.6 eV for the CT-band energy in Fig. 1.

Figure 2(b) also shows the PLE ($\lambda_{em} = 355$ nm) and PL ($\lambda_{ex} = 297$ nm) spectra of $LiScGeO_4$:$0.005Bi^{3+}$ recorded at RT. Different from that in Ref. 24, a new excitation band peaked at ~230 nm is observed. To further unravel the nature of Bi^{3+} luminescence, the photoluminescence emission and excitation spectra were measured in the spectral range from 125 to 550 nm at 10 K as shown in Fig. 2(d). Monitored at 355 or 385 nm, the excitation spectrum shares five excitation bands peaked at ~169, 196.6, 231.9, 297.6, and 308 nm. Like in Ref. 27, the low-energy excitation bands peaked at 297.6 and 308 nm will be assigned to the Bi^{3+} Jahn–Teller split $^1S_0 \rightarrow {}^3P_1$ transition, i.e., Bi^{3+} A-band. The excitation band located at 231.9 nm (5.35 eV) will be assigned in Sec. III to the charge transfer from Bi^{3+} to the conduction band of $LiScGeO_4$, i.e., the Bi^{3+} D-band.[22] The excitation band located at 196.6 nm will be attributed to the Bi^{3+} $^1S_0 \rightarrow {}^1P_1$ transition, i.e., the Bi^{3+} C-band. The excitation band located at ~169 nm will remain unassigned. Upon 232.6 or 290 nm excitation, an emission band peaked at ~359 nm with a full

width at half maximum (FWHM) of 34 nm appears, which is attributed to the typical Bi^{3+} $^3P_1 \rightarrow {}^1S_0$ transition. The data were used to draw the Bi^{3+} levels and the observed transitions in the bandgap of $LiScGeO_4$ in Fig. 1.

Figure 2(e) shows the PLE and PL spectra of $LiScGeO_4$:$0.005Pr^{3+}$ at 10 K. Upon 190 nm excitation, not only the broad host exciton emission band peaked near 501 nm but also the typical Pr^{3+} 4f → 4f emissions are observed. Monitored at 602 nm, the excitation spectrum is composed of three excitation bands located at 190, 240, and 259 nm. The 190 nm excitation band is also observed for the undoped host in Fig. 2(a) and therefore is attributed to the host exciton creation (E^{ex}). The two excitation bands located at ~259 nm (4.79 eV) and ~240 nm (5.17 eV) will be attributed to the first and second Pr^{3+} 4f → 5d transitions. Based on the VRBE diagram, we expect the direct excitation from Pr^{3+} to the conduction band (CB), or the Intervalence Charge Transfer band (IVCT), near 4.7 eV or 263 nm. It is probably hidden underneath the more intense $5d_1$ band.

Figure 2(f) shows the PLE and PL spectra of $LiScGeO_4$:$0.005Tb^{3+}$ at 10 K. Upon a 193 nm excitation, both the broad exciton emission band and the characteristic Tb^{3+} $^5D_4 \rightarrow {}^7F_j$ line emissions appear. Upon a 250 nm excitation, the exciton emission is absent and only the typical Tb^{3+} $^5D_4 \rightarrow {}^7F_j$ emissions emerge. Monitored at 551 nm, the excitation spectrum is composed of six excitation bands located at ~167.5, 192, 232, 250, 268.5, and 300 nm. The excitation band peaked at ~167.5 nm is of unknown origin and also observed for $LiScGeO_4$:$0.005Bi^{3+}$ in Fig. 2(d). Like in Figs. 2(a) and 2(e), the excitation band located at ~192 nm (6.46 eV) is attributed to the host exciton creation (E^{ex}). The excitation bands peaked at 300 nm (4.13 eV) and 250 nm (4.96 eV) will be assigned to the first spin forbidden and spin allowed 4f → 5d transitions. The excitation band peaked at 232 nm (5.35 eV) will be tentatively assigned to the second spin allowed 4f → 5d transition. The excitation band peaked near 268.5 nm (4.62 eV) will be tentatively assigned to the intervalence charge transfer (IVCT) from the Tb^{3+} ground state to the conduction band (CB), i.e., $Tb^{3+} \rightarrow CB$ IVCT.

B. Identifying recombination, luminescence centers, and trapping processes of charge carriers in $LiScGeO_4$

To unravel recombination and trapping processes of charge carriers, Bi^{3+} or/and lanthanides Ln^{3+} (Ln = Tb, Eu, or Pr) doped $LiScGeO_4$ storage phosphors were first studied. Figures 3(a) and 3(b) show the room temperature (RT) isothermal decay spectra of $LiScGeO_4$:$0.005Tb^{3+}$ and $LiScGeO_4$:$0.005Tb^{3+},0.001Eu^{3+}$ after being illuminated by 254 nm UV-light for 60 s. Tb^{3+} appears as the recombination and luminescence center. Figures 3(c) and 3(d) present the RT isothermal decay spectra for $LiScGeO_4$:$0.005Pr^{3+}$ and $LiScGeO_4$:$0.005Pr^{3+},0.001Eu^{3+}$ after 254 nm UV-light charging for 60 s. Pr^{3+} with the typical 4f → 4f emissions emerges as the recombination and luminescence center. Figure 3(e) shows the RT isothermal decay spectra for $LiScGeO_4$:$0.003Bi^{3+}$ charged by 254 nm UV-light with a duration of 60 s. Bi^{3+} with the A-band ($^3P_1 \rightarrow {}^1S_0$) emission works as the recombination and emission center. Figure 3(f) shows the RT isothermal decay spectra of $LiScGeO_4$:$0.003Bi^{3+},0.001Eu^{3+}$ after being illuminated by 254 nm UV-light for 60 s. The Bi^{3+} A-band and characteristic Eu^{3+} $^5D_0 \rightarrow {}^7F_j$ (j = 0–6) emissions are observed. Bi^{3+} appears as the recombination and emission center. Possibly, the Eu^{3+} emissions are realized by an energy transfer process from Bi^{3+} to Eu^{3+}, which is partly evidenced by the PLE ($\lambda_{em} = 612$ and 360 nm)
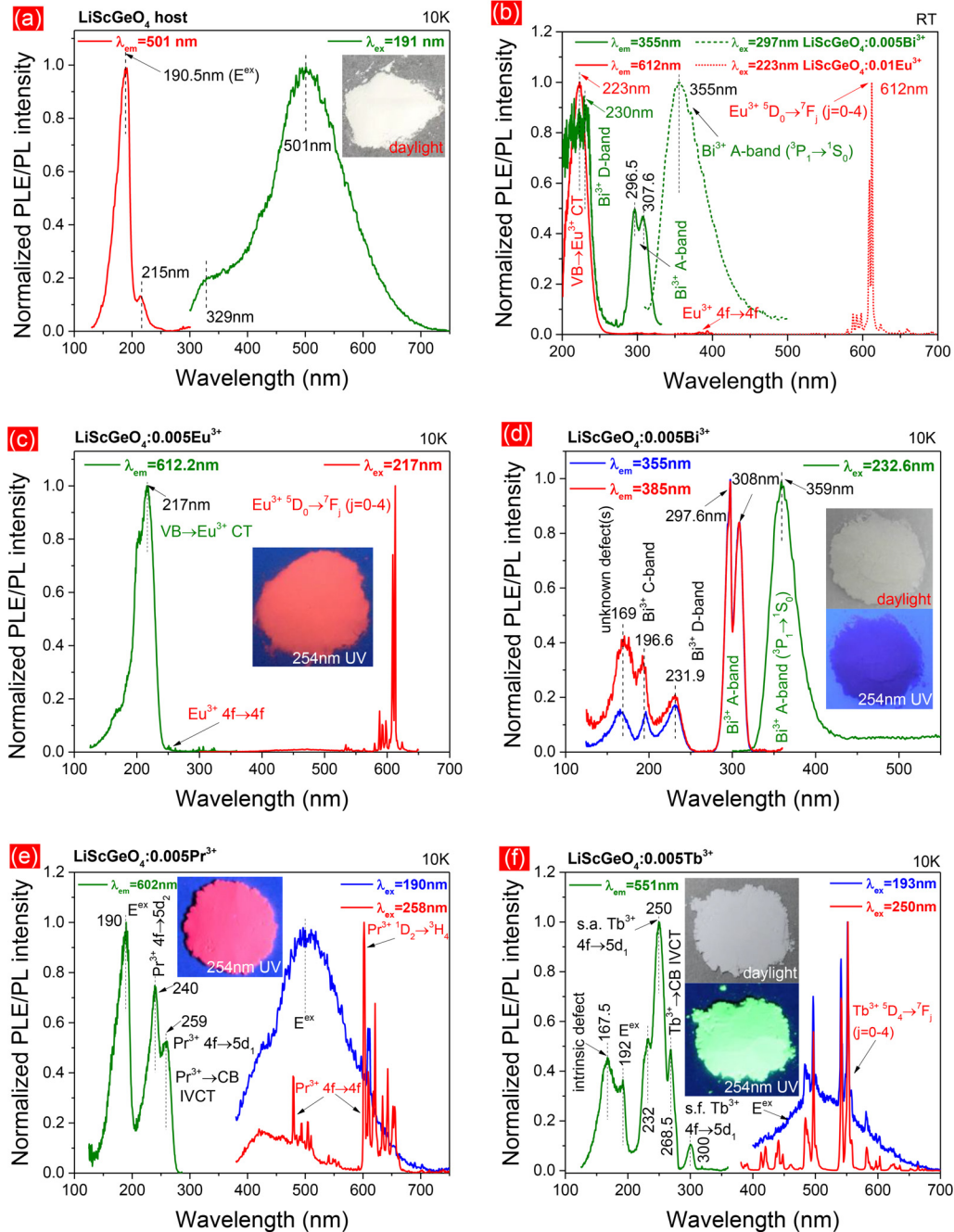
FIG. 2. (a)–(f) Photoluminescence excitation (PLE) and emission (PL) spectra for undoped, Eu^{3+}, Bi^{3+}, Pr^{3+}, or Tb^{3+} single doped $LiScGeO_4$ measured at room temperature (RT) or 10 K. The insets show the photographs of the synthesized phosphors under daylight or upon a Hg lamp (254 nm) UV-light illumination in the dark. These PLE and PL spectra were normalized for better comparison. The compound compositions, monitored excitation, emission wavelengths, and experimentally observed transitions with possible assignments have been specifically denoted in panels (a)–(f).

and PL ($\lambda_{ex} = 298$ nm) spectra of $LiScGeO_4$:0.003Bi^{3+}, 0.001Eu^{3+} as shown in Fig. S6(c).

Figure 3(g) compares the thermoluminescence excitation (TLE) plot recorded at RT with the photoluminescence excitation (PLE)

spectrum ($\lambda_{em} = 355$ nm) of $LiScGeO_4$:0.003Bi^{3+} at 10 K. The traps in $LiScGeO_4$:0.003Bi^{3+} can be filled via the Bi^{3+} D-band excitation and not via the Bi^{3+} A-band excitation despite its intense excitation intensity. Figure 3(h) compares the TLE plot with the PLE spectrum

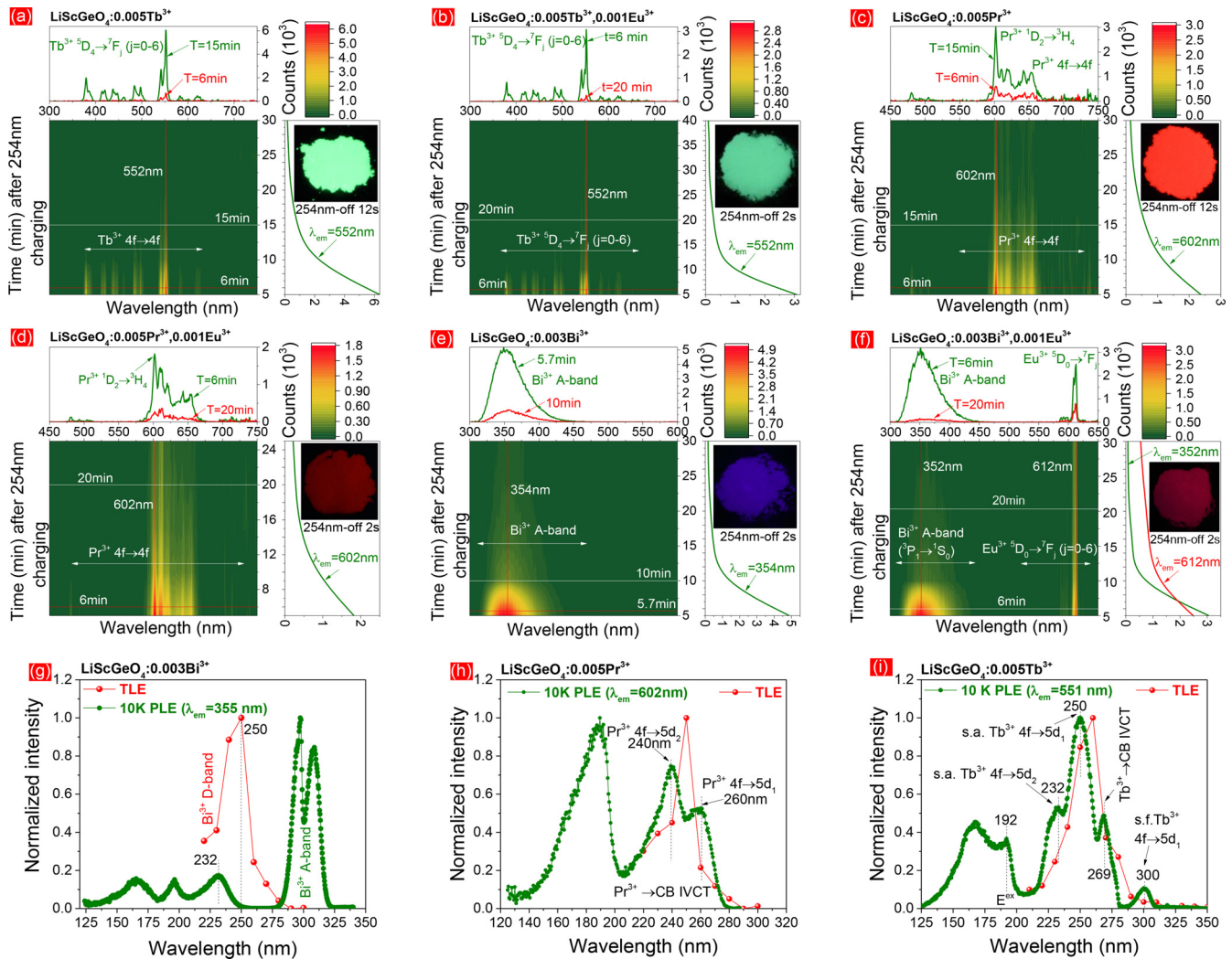**FIG. 3.** Room temperature (298 K) isothermal decay spectra as a function of time after a 254 nm UV-light charging for (a) $LiScGeO_4$:$0.005Tb^{3+}$, (b) $LiScGeO_4$: $0.005Tb^{3+}$,$0.001Eu^{3+}$, (c) $LiScGeO_4$:$0.005Pr^{3+}$, (d) $LiScGeO_4$:$0.005Pr^{3+}$,$0.001Eu^{3+}$, (e) $LiScGeO_4$:$0.003Bi^{3+}$, and (f) $LiScGeO_4$:$0.003Bi^{3+}$,$0.001Eu^{3+}$. A comparison of thermoluminescence excitation (TLE) and photoluminescence excitation (PLE) spectra for (g) $LiScGeO_4$:$0.003Bi^{3+}$, (h) $LiScGeO_4$:$0.005Pr^{3+}$, and (i) $LiScGeO_4$:$0.005Tb^{3+}$. The insets in (a)–(f) show the afterglow photographs after 254 nm UV-light charging.

($\lambda_{em} = 602$ nm) of $LiScGeO_4$:$0.005Pr^{3+}$ at 10 K. The traps in $LiScGeO_4$:$0.005Pr^{3+}$ can be charged via the Pr^{3+} 4f → 5d and the Pr^{3+} → CB IVCT excitation. Figure 3(i) compares the TLE plot with the PLE spectrum ($\lambda_{em} = 551$ nm) of $LiScGeO_4$:$0.005Tb^{3+}$ at 10 K. The traps in $LiScGeO_4$:$0.005Tb^{3+}$ can be filled through the Tb^{3+} → CB IVCT and the excitation from Tb^{3+} ground state to its excited 5d states.

C. Evidencing Eu^{3+} as a deep electron trap and Bi^{3+} and Tb^{3+} as hole trapping and recombination centers in $LiSc_{1-x}Lu_xGeO_4$

Figure 1 predicts that Eu^{3+} works as an about 1.25 eV deep electron trapping center, Tb^{3+}, Pr^{3+}, and Bi^{3+}, respectively, work as about 2.15, 2.19, or 1.5 eV deep hole trapping centers in $LiScGeO_4$. A

combination of Eu^{3+} with Tb^{3+}, Pr^{3+}, or Bi^{3+} may then lead to good $LiScGeO_4$ storage phosphor properties. To verify this prediction, Bi^{3+} or/and lanthanides Ln^{3+} (Ln = Tb, Pr, or Eu) doped $LiScGeO_4$ compounds were synthesized. Their TL glow curves were recorded at a heating rate (β) of 1 K/s after exposure to x-rays and are shown in Fig. 4(a). Compared with Bi^{3+} single doped $LiScGeO_4$:$0.003Bi^{3+}$ or Pr^{3+} single doped $LiScGeO_4$:$0.005Pr^{3+}$, a new TL glow band peaked near 461 K appears in the temperature range from ~350 to ~550 K. As illustrated in the inset of Fig. 4(a), it will be attributed to the electron liberation from Eu^{2+} during thermal stimulation and recombination with the holes captured at Bi^{4+}, Tb^{4+}, or Pr^{4+}, generating characteristic Bi^{3+} $^3P_1 \rightarrow ^1S_0$, Tb^{3+}, and Pr^{3+} 4f → 4f emissions. The ratios named as (n1; n2) of the integrated TL intensities from 303 to 650 K for the Bi^{3+} or/and lanthanides doped $LiScGeO_4$ compounds to that of the state-of-the-art storage phosphors BaFBr(I):Eu^{2+} (n1) or
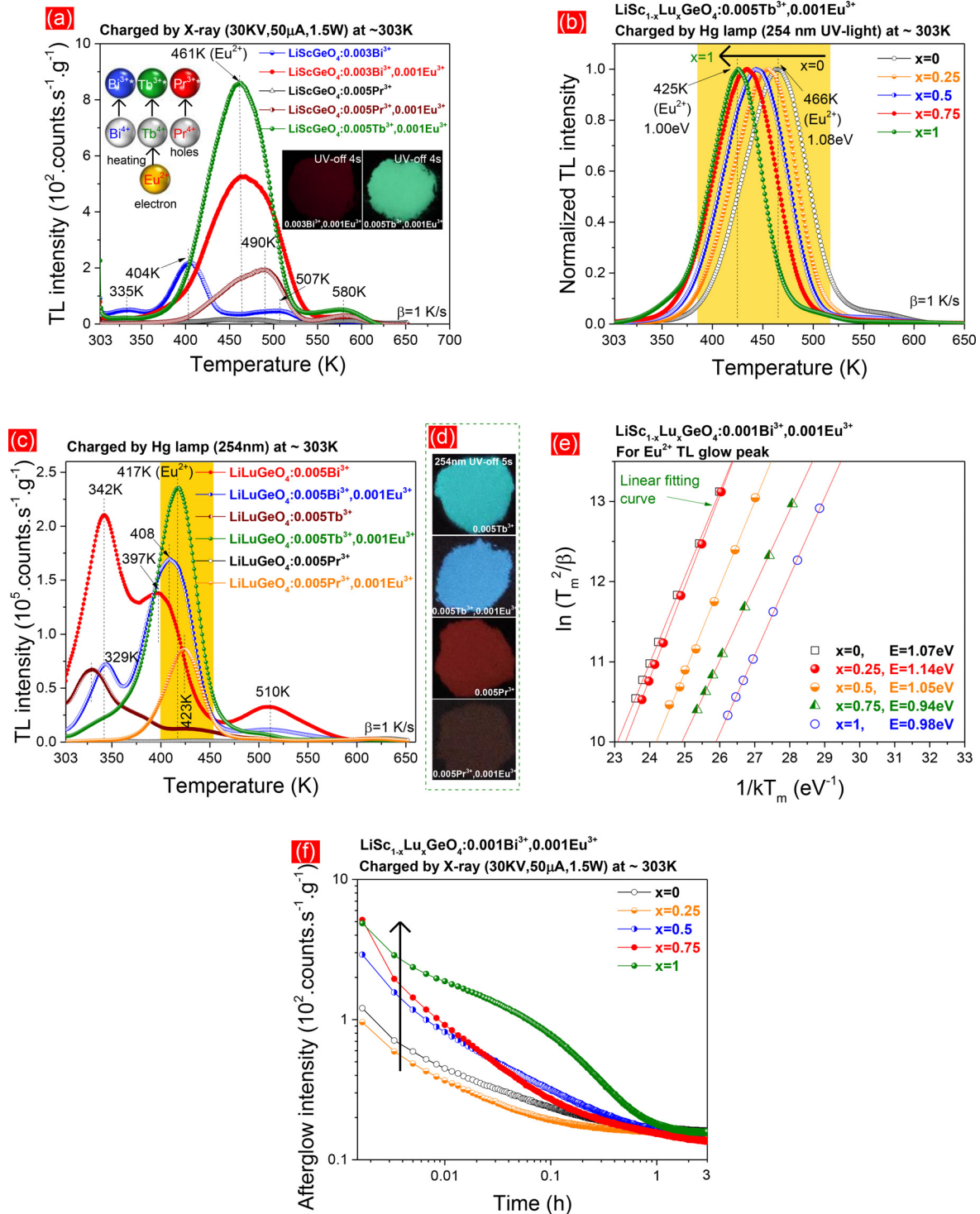
FIG. 4. TL glow curves recorded at a heating of 1 K/s for x-ray or 254 nm UV-light irradiated (a) Bi^{3+} or/and lanthanides doped $LiScGeO_4$, (b) $LiSc_{1-x}Lu_xGeO_4$: $0.005Tb^{3+},0.001Eu^{3+}$, and (c) Bi^{3+} or/and lanthanides doped $LiLuGeO_4$. (e) Variable heating rate plots and (f) RT isothermal decay curves after x-ray illumination for $LiSc_{1-x}Lu_xGeO_4:0.001Bi^{3+},0.001Eu^{3+}$ (x = 0–1). The insets in (a) and (d) show the afterglow photographs after 254 nm UV-light illumination in the dark.

Al$_2$O$_3$:C chip (n2) are provided in Table S1 and they are substantially lower than 1.

To further evidence that Eu^{3+} acts as a deep electron trapping center, Eu^{3+} co-doped LiSc$_{1-x}$Lu$_x$GeO$_4$ solid solutions were synthesized. Figure 4(b) first shows the TL glow curves of LiSc$_{1-x}$Lu$_x$GeO$_4$:0.005Tb^{3+}, 0.001Eu^{3+} after being illuminated by 254 nm UV-light where Tb^{3+} acts as the recombination and luminescence center. With increasing x, the Eu^{2+} TL band gradually shifts from 466 K for x = 0 to 425 K for x = 1. The same applies to Bi^{3+},Eu^{3+}-codoped LiSc$_{1-x}$Lu$_x$GeO$_4$ in Fig. S10. The systematic shifting of the Eu^{2+} TL glow band toward a lower temperature will be assigned to decreased activation energy for electron liberation from Eu^{2+} because of conduction band lowering with rising x in LiSc$_{1-x}$Lu$_x$GeO$_4$.

Figure 4(c) compares the TL glow curves measured at $\beta = 1$ K/s for Bi^{3+} or/and lanthanides doped LiLuGeO$_4$ after exposure to 254 nm UV-light in the dark. Compared with LiLuGeO$_4$:0.005Tb^{3+}, LiLuGeO$_4$:0.005Bi^{3+}, or LiLuGeO$_4$:0.005Pr^{3+}, a new and common TL glow band peaked near 417 K emerges in the temperature range from ~375 to ~475 K for the Eu^{3+} co-doped samples. Like in Fig. 4(a), it is attributed to the electron release from Eu^{2+} and recombination with the holes trapped at Bi^{4+}, Pr^{4+}, and Tb^{4+}.

To determine the trapping depths, the TL glow curves for x-ray irradiated LiSc$_{1-x}$Lu$_x$GeO$_4$:0.001Bi^{3+},0.001Eu^{3+} were recorded at different heating rates and are shown in Fig. S18. Assuming that a first-order thermoluminescence recombination kinetics applies, one can estimate the trapping depth by utilizing a variable heating rate plot with the following formula:[28]

$$\ln\left(\frac{T_m{}^2}{\beta}\right) = \frac{E}{kT_m} + \ln\left(\frac{E}{ks}\right),\qquad(1)$$

in which E means the trapping depth, s denotes the frequency factor (s^{-1}), β denotes the utilized heating rate, k is the Boltzmann constant, and T$_m$ is the temperature (K) at the maximum of the TL glow peak. Figure 4(e) presents the variable heating rate plots of the Eu^{2+} TL glow bands for LiSc$_{1-x}$Lu$_x$GeO$_4$:0.001Bi^{3+}, 0.001Eu^{3+}. The trapping depths can be deduced from the slopes of the linear fitting equations, and the frequency factors can be derived from the intercepts with the relation of ln(E/ks). These obtained values are provided in the legend of Fig. 4(e) and Table S2.

Figure 4(f) shows RT isothermal decay curves of LiSc$_{1-x}$Lu$_x$GeO$_4$:0.001Bi^{3+},0.001Eu^{3+} after x-ray charging with a duration of 300 s. With increasing x, increased afterglow intensity appears. The same applies to LiLuGeO$_4$:0.005Tb^{3+},0.001Eu^{3+} in Fig. S11. More than 3 h Tb^{3+} ^{5}D$_4 \rightarrow ^7$F$_j$ or Bi^{3+} A-band afterglow can be detected in x-ray charged LiLuGeO$_4$:0.005Tb^{3+},0.001Eu^{3+} and LiLuGeO$_4$:0.001Bi^{3+},0.001Eu^{3+}.

D. Evaluating LiSc$_{1-x}$Lu$_x$GeO$_4$:M^{3+},Eu^{3+} (M = Bi or Tb) as dosimeters for radiation detection

The developed LiSc$_{1-x}$Lu$_x$GeO$_4$:M^{3+},Eu^{3+} (M = Bi or Tb) storage phosphors have been evaluated as ionizing radiation dosimeters.

Figure 5(a) presents the TL glow curves of LiScGeO$_4$:0.005Tb^{3+},0.001Eu^{3+} irradiated by x-rays with different durations from 30 to 600 s. The integrated TL intensities as a function of x-ray exposure time are provided in the inset of Fig. 5(a). The same

applies to LiScGeO$_4$:0.001Bi^{3+},0.001Eu^{3+} and LiLuGeO$_4$:0.001Bi^{3+}, 0.001Eu^{3+} as given in Fig. S19.

Figures 5(b) and 5(c) give the TL glow curves of LiScGeO$_4$:0.005Tb^{3+},0.001Eu^{3+} and LiSc$_{0.25}$Lu$_{0.75}$GeO$_4$:0.001Bi^{3+},0.001Eu^{3+}, which were first irradiated by x-rays for 200 s and then with different delay durations from 0 to 3600 s prior to TL-readout. The ratios of the integrated TL intensities with different delay durations to that of only with x-ray charging are listed as percentages in the legends of Figs. 5(b) and 5(c). After 1 h delay, the TL intensity remains 91% for LiScGeO$_4$:0.005Tb^{3+},0.001Eu^{3+} and 86.5% for LiSc$_{0.25}$Lu$_{0.75}$GeO$_4$:0.001Bi^{3+},0.001Eu^{3+}. It means that the stored electrons at Eu^{2+} are not rapidly released at RT and stored information fading is slow. The same applies to other Bi^{3+} and/or lanthanides doped LiSc$_{1-x}$Lu$_x$GeO$_4$ storage phosphors in Fig. S20.

Figures 5(d) and 5(e) show the TL glow curves for LiScGeO$_4$:0.005Tb^{3+},0.001Eu^{3+} and LiSc$_{0.25}$Lu$_{0.75}$GeO$_4$:0.001Bi^{3+},0.001Eu^{3+}, which were first irradiated by 254 nm UV-light for 20 s and then illuminated by different energy photons with tens or different durations. The ratios of the integrated TL intensities with additional photon stimulation to that of only with 254 nm UV-light charging are displayed as percentages in the legends of Figs. 5(d) and 5(e). The electrons trapped at Eu^{2+} can be liberated by light stimulation in a wide range from 365 nm UV-light to 850 nm infrared light. The similar applies to other Bi^{3+} and/or lanthanides doped LiSc$_{1-x}$Lu$_x$GeO$_4$ as shown in Figs. S21 and S22.

Figure 5(f) gives the RT isothermal decay curves of LiSc$_{0.25}$Lu$_{0.75}$GeO$_4$:0.001Bi^{3+},0.001Eu^{3+} and LiSc$_{0.25}$Lu$_{0.75}$GeO$_4$:0.005Tb^{3+},0.001Eu^{3+} after exposure to x-rays with a duration of 260 s. The afterglow intensities during the first 60 s are very weak. About 76 or 35 times stronger stimulated luminescence appears in Fig. 5(f) when the 850 nm infrared laser is switched on. This feature evidence that the electrons stored at Eu^{2+} are released by means of an efficient optically stimulated luminescence process.

For application, charge carrier storage capacity is also important. The new LiSc$_{0.25}$Lu$_{0.75}$GeO$_4$: 0.001Bi^{3+},0.001Eu^{3+} solid solution was therefore optimized by adjusting the synthesis condition. Figure 6(a) compares the TL glow curves for 200 s x-ray irradiated commercial BaFBr(I):Eu^{2+}, Al$_2$O$_3$:C chip, and the LiSc$_{0.25}$Lu$_{0.75}$GeO$_4$:0.001Bi^{3+},0.001Eu^{3+} synthesized at 1150 °C for 6 h or 10 h. The ratios (n1; n2) of the integrated TL intensities from 303 to 650 K of the synthesized LiSc$_{0.25}$Lu$_{0.75}$GeO$_4$:0.001Bi^{3+},0.001Eu^{3+} to that of the commercial BaFBr(I):Eu^{2+} or Al$_2$O$_3$:C chip are given in the legend of Fig. 6(a). The TL intensity of the optimized LiSc$_{0.25}$Lu$_{0.75}$GeO$_4$:0.001Bi^{3+},0.001Eu^{3+} prepared at 1150 °C for 10 h is about two times higher than that of the commercial x-ray storage phosphor BaFBr(I):Eu^{2+}. It means that it has excellent charge carrier storage capacity during x-ray exposure. In Fig. 6(a), a TL glow peak located at ~361 K appears in the temperature range from 303 to 425 K in the x-ray charged BaFBr(I):Eu^{2+}, which is close to RT. It means that the fading of stored charge carriers occurs in the BaFBr(I):Eu^{2+} by means of the Eu^{2+} afterglow at RT. The Eu^{2+} TL glow peak is well above RT, and weak fading is expected in the optimized LiSc$_{0.25}$Lu$_{0.75}$GeO$_4$:0.001Bi^{3+}, 0.001Eu^{3+}.

Figures 6(b) and 6(c) give the 2D contour plots of the above 100 K TL emission (TLEM) spectra for the optimized LiSc$_{0.25}$Lu$_{0.75}$GeO$_4$:0.001Bi^{3+},0.001Eu^{3+} and LiSc$_{0.25}$Lu$_{0.75}$GeO$_4$:0.005Tb^{3+},0.001Eu^{3+} irradiated by x-rays. It appears that Bi^{3+} with the ^{3}P$_1 \rightarrow ^1$S$_0$ emission and Tb^{3+} with its typical ^{5}D$_4 \rightarrow ^7$F$_j$ emissions act as the recombination and emission centers during TL-readout from 100 to 600 K.
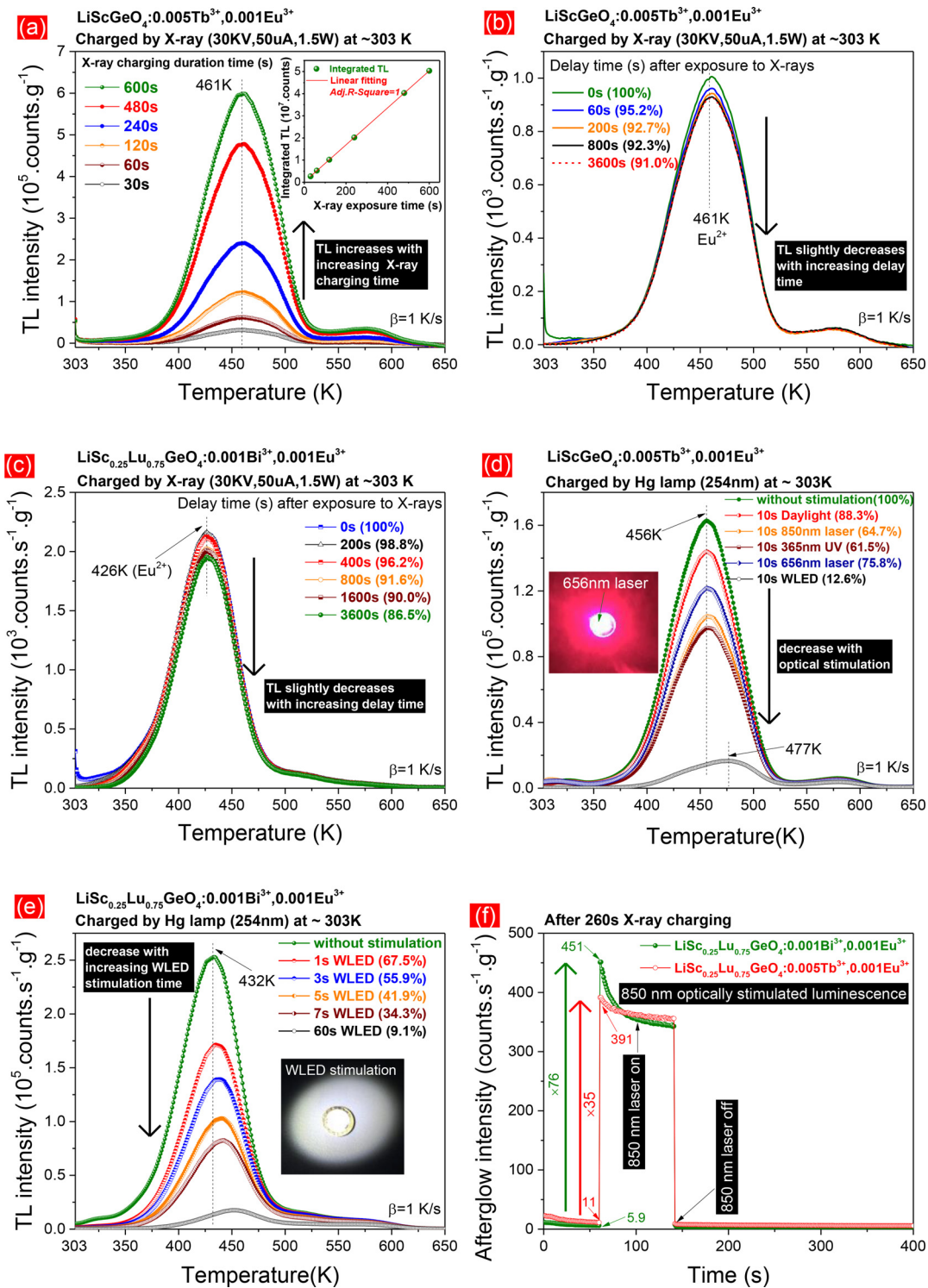
FIG. 5. (a) X-ray dose dependent TL glow curves, (b) and (c) TL fading characteristics after x-ray charging, and (d) and (e) TL glow curves first irradiated by 254 nm UV-light for 20 s and then illuminated by different energy photon with different durations for LiScGeO$_4$:0.005Tb^{3+},0.001Eu^{3+} and LiSc$_{0.25}$Lu$_{0.75}$GeO$_4$:0.001Bi^{3+}, 0.001Eu^{3+}. (f) RT isothermal decay curves first irradiated by x-ray for 260 s and then with 850 nm infrared laser stimulation for LiSc$_{0.25}$Lu$_{0.75}$GeO$_4$:0.001Bi^{3+},0.001Eu^{3+} and LiSc$_{0.25}$Lu$_{0.75}$GeO$_4$:0.005Tb^{3+},0.001Eu^{3+}.
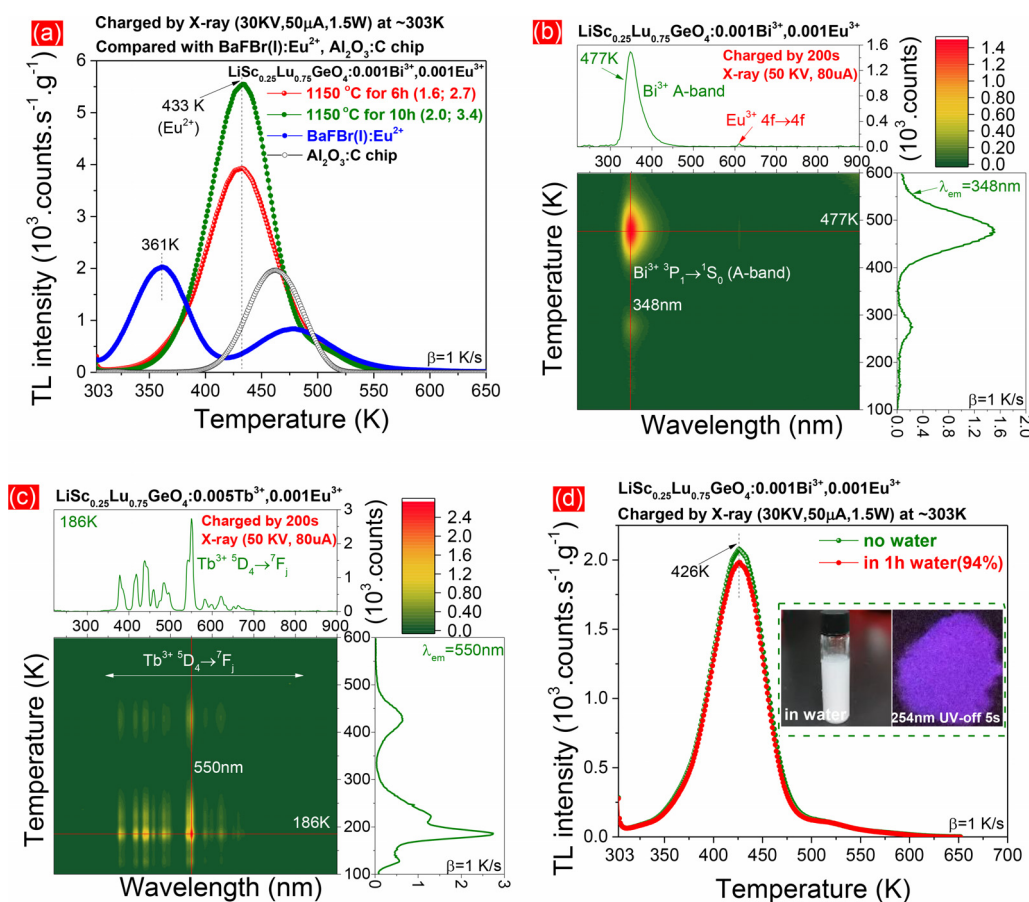
FIG. 6. (a) Above 303 K TL glow curves at $\beta = 1$ K/s for x-ray irradiated $LiSc_{0.25}Lu_{0.75}GeO_4:0.001Bi^{3+}$, $0.001Eu^{3+}$ synthesized at 1150 °C for 6 h or 10 h. (b) (c) Above 100 K TL emission spectra (TLEM) recorded at $\beta = 1$ K/s after x-ray charging for the optimized $LiSc_{0.25}Lu_{0.75}GeO_4:0.001Bi^{3+},0.001Eu^{3+}$ and $LiSc_{0.25}Lu_{0.75}GeO_4: 0.005Tb^{3+},0.001Eu^{3+}$ synthesized at 1150 °C for 10 h. (d) TL glow curves of the x-ray irradiated $LiSc_{0.25}Lu_{0.75}GeO_4:0.001Bi^{3+},0.001Eu^{3+}$ after exposure to water for 1 h.

For practical application, stability against water is also important for the synthesized compounds. Figure 6(d) gives the TL glow curves of x-ray irradiated $LiSc_{0.25}Lu_{0.75}GeO_4:0.001Bi^{3+},0.001Eu^{3+}$ without and after exposure to water for 1 h. The TL intensity remains at 94% after 1 h of exposure to water. It means that the synthesized $LiSc_{0.25}Lu_{0.75}GeO_4:0.001Bi^{3+},0.001Eu^{3+}$ solid solution has excellent stability against water exposure.

E. Evaluating $LiSc_{1-x}Lu_xGeO_4:M^{3+},Eu^{3+}$ (M = Bi or Tb) for non-real-time force recording

Charge carrier trapping with mechanical stimulation is interesting for non-real-time force recording application, and the synthesized $LiSc_{1-x}Lu_xGeO_4:M^{3+},Eu^{3+}$ (M = Bi or Tb) were therefore studied.

Figure 7(a) and S23 give the TL glow curves measured at $\beta = 1$ K/s for the synthesized solid solutions $LiSc_{0.75}Lu_{0.25}GeO_4: 0.005Tb^{3+},0.001Eu^{3+}$, $LiSc_{0.5}Lu_{0.5}GeO_4:0.001Bi^{3+},0.001Eu^{3+}$, and the optimized $LiSc_{0.25}Lu_{0.75}GeO_4:0.001Bi^{3+},0.001Eu^{3+}$ charged only by grinding in an agate mortar with a pestle for different durations from 0 to 600 s. A TL glow band peaked near 630 K emerges in the temperature

range from ∼500 to ∼723 K in Fig. 7(a). Figure 7(b) shows that TL intensity increases linearly with increasing the grinding time in the above three samples. The phenomenon of charge carrier storage by mechanical excitation can be repeatedly observed in the Eu^{3+} co-doped $LiSc_{0.75}Lu_{0.25}GeO_4$ and $LiSc_{0.5}Lu_{0.5}GeO_4$ in Fig. 7(a) and S23. It also repeatedly appears in other $LiSc_{1-x}Lu_xGeO_4:M^{3+},Eu^{3+}$ (M = Bi or Tb) storage phosphors as demonstrated in Figs. S24 and S25. The commercial $ZnS:Mn^{2+}$ mechanoluminescence material was also ground in an agate mortar with a pestle for 300 s in the dark. However, thermoluminescence was not detected in the ground $ZnS:Mn^{2+}$ when it was heated from 300 to ∼700 K at a heating rate of 1 K/s in the dark.

To unravel the nature of the traps for force induced charge carrier storage, Fig. 7(c) compares the thermoluminescence glow curves recorded at $\beta = 1$ K/s for $LiSc_{0.25}Lu_{0.75}GeO_4:0.005Tb^{3+},0.001Eu^{3+}$, which was charged by grinding for 210 s or by illumination of 254 nm UV-light for 20 s or x-rays for 200 s. Different from that by charging with 254 nm UV-light or x-rays, 210 s grinding leads to a well above 426 K TL glow band peaked near 656 K in the temperature range from 525 to 723 K. Figure 7(d) gives the TL glow curves of $LiSc_{0.25}Lu_{0.75}GeO_4:0.005Tb^{3+},0.001Eu^{3+}$ charged by grinding in an agate
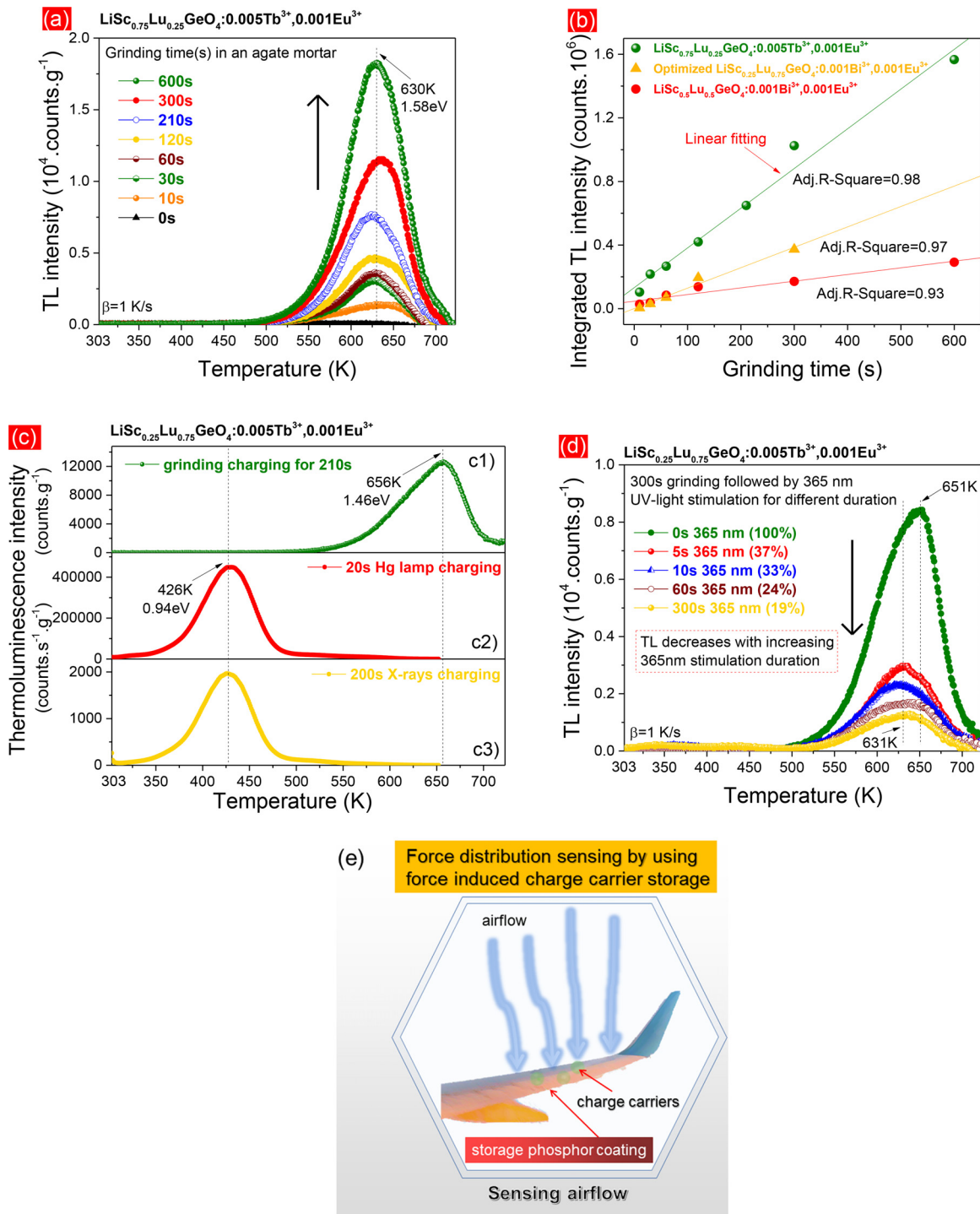
FIG. 7. (a) TL glow curves measured at $\beta = 1$ K/s and (b) a comparison of integrated TL intensities from 303 to $\sim$723 K for LiSc$_{0.75}$Lu$_{0.25}$GeO$_4$:0.005Tb^{3+},0.001Eu^{3+}, LiSc$_{0.5}$Lu$_{0.5}$GeO$_4$:0.001Bi^{3+},0.001Eu^{3+}, and the optimized LiSc$_{0.25}$Lu$_{0.75}$GeO$_4$:0.001Bi^{3+},0.001Eu^{3+} with different grinding times in an agate mortar. (c) TL glow curves for LiSc$_{0.25}$Lu$_{0.75}$GeO$_4$:0.005Tb^{3+},0.001Eu^{3+} charged by 210 s grinding, 20 s 254 nm UV-light, or 200 s x-ray illumination in the dark. (d) TL glow curves of LiSc$_{0.25}$Lu$_{0.75}$GeO$_4$:0.005Tb^{3+},0.001Eu^{3+} charged by 300 s grinding and then stimulated by 365 nm UV-light for different durations. (e) Demonstration on the proof-of-concept force distribution sensing by using the force induced charge carrier storage feature.

mortar for 300 s and then stimulated by 365 nm UV-light for different durations from 0 to 300 s. The ratios of the integrated TL intensities from 303 to 723 K by additional 365 nm UV-light stimulation to that of only with grinding for 300 s are provided as percentages in the legend of Fig. 7(d). The amount of the stored charge carriers by mechanical stimulation decreases with increasing the illumination duration of the 365 nm UV-light. The same applies to $LiSc_{0.25}Lu_{0.75}GeO_4{:}0.005Tb^{3+},0.001Eu^{3+}$ with additional WLED or a 656 nm laser stimulation in Fig. S26.

Since the new TL band created by mechanical stimulation is well above RT, the charge carriers can be stably stored in traps. It means that the force induced charge carrier storage feature has potential use in force distribution sensing application, which is schematically demonstrated in Fig. 7(e). The wing of a plane is covered by a storage phosphor based coating film. Charge carriers formed by mechanical excitation with airflow are stored in traps in storage phosphors. During a 365 nm UV-light exposure, it is expected that the stored charge carriers are liberated from traps by optically stimulated luminescence to generate an image to show the excitation force distribution.

F. Evaluating $LiSc_{1-x}Lu_xGeO_4{:}Tb^{3+},Eu^{3+}$ for anti-counterfeiting and x-ray imaging applications

The $LiLuGeO_4{:}0.005Tb^{3+},0.001Eu^{3+}$ and $LiScGeO_4{:}0.003Pr^{3+}$ powder phosphors are white under daylight. They can be used with ink to print labels like a QR code on a sheet of normal white paper. Confidential information can be hidden by means of a designed QR code. The QR code is not visible under daylight because it is white. The hidden confidential information can only be readout by scanning the afterglow QR code with a smart phone in the dark. To the best of our knowledge, white afterglow is rarely reported but it can be used as a special illumination source to correctly show the colors of objects in the dark. Therefore, color-tailorable and white afterglow phosphors have unique use for anti-counterfeiting application. The above idea is demonstrated by using the developed $LiLuGeO_4{:}0.005Tb^{3+},0.001Eu^{3+}$ and $LiScGeO_4{:}0.003Pr^{3+}$ storage phosphors or a mixture of both. Since charge carriers in traps can be liberated by a wide range 365–850 nm infrared light, a smart afterglow QR code can be designed by selectively erasing the hidden information for advanced anti-counterfeiting application.

The information of "Vacuum-referred binding energies of bismuth and lanthanide levels" was hidden by means of a QR code. The $LiLuGeO_4{:}0.005Tb^{3+},0.001Eu^{3+}$, $LiScGeO_4{:}0.003Pr^{3+}$, or a mixture of both storage phosphors was first sifted by a 200 mesh screen. The powder was then homogeneously dispersed in a transparent ink solution to print the QR code or the Einstein photograph on a sheet of paper in Figs. 8(a1), 8(a4), 8(b1), 8(b4), and 8(c1) by using a screen printing technique. Green QR code and Einstein photograph are visible in the dark in Figs. 8(a3) and 8(a5) because of the RT thermally stimulated

Colour-tailorable afterglow with information storage for anti-counterfeiting application
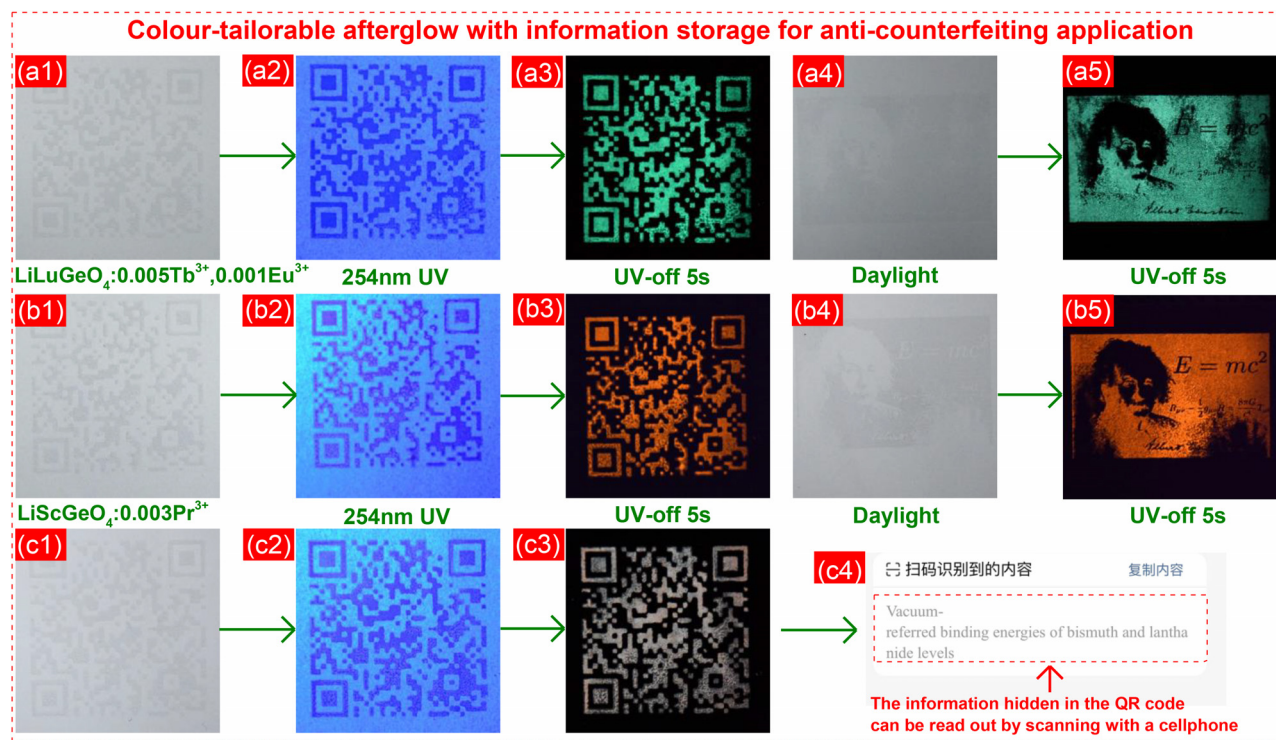
FIG. 8. Photos on rows (a)–(c), pertain to a sheet of paper printed with a QR code or a photograph of Albert Einstein, respectively, with columns (a1), (a4), (b1), (b4), and (c1) the appearance during daylight, columns (a2), (b2), (c2) under Hg lamp illumination, and columns (a3), (a5), (b3), (b5), and (c3) the afterglow appearance at 5 s after stopping Hg lamp illumination. The QR code and the Einstein photograph were printed on papers by a screen printing technique with the developed $LiLuGeO_4{:}0.005Tb^{3+},0.001Eu^{3+}$ for (a1) and (a4), the $LiScGeO_4{:}0.003Pr^{3+}$ for (b1) and (b4), or with a mixture of both storage phosphors for (c1). (c4) The afterglow QR codes in (a3), (b3), and (c3) can be scanned by a mobile phone to readout the hidden information.
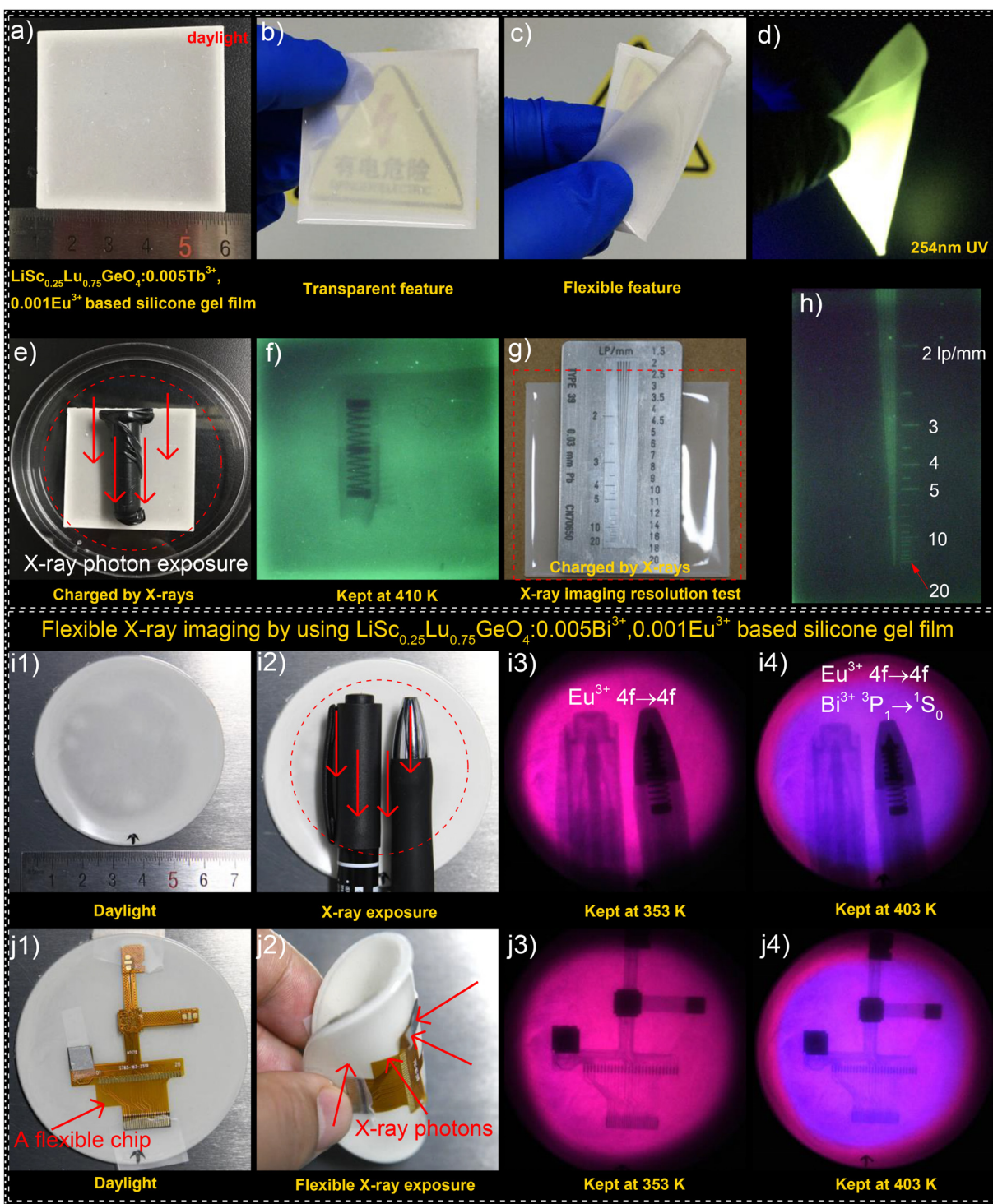
FIG. 9. (a)–(d) and (i1) The developed $LiSc_{0.25}Lu_{0.75}GeO_4:0.005Tb^{3+},0.001Eu^{3+}$ and $LiSc_{0.25}Lu_{0.75}GeO_4: 0.005Bi^{3+},0.001Eu^{3+}$ storage phosphors were dispersed into silicone gel to produce transparent and flexible x-ray imaging films. (e)–(j4) Proof-of-concept x-ray imaging and resolution test by utilizing the produced imaging films. In panels (e), (g), (i2), and (j2), the film was placed underneath a capsule with a hidden metal spring, a standard Pb-based x-ray imaging resolution test plate, two ball-point pens, or a flexible electronic chip. They were perpendicularly exposed to x-rays at room temperature in the dark. After x-ray exposure, these objects were removed from the film. x-ray imaging photographs were then obtained when the film was kept at 410, 353, or 403 K in the dark.

Tb^{3+} $^5D_4 \rightarrow$ ^7F_j emissions from LiLuGeO$_4$:0.005Tb^{3+},0.001Eu^{3+} charged by 254 nm UV-light. Red QR code and Einstein photograph emerge in the dark in Figs. 8(b3) and 8(b5) due to the Pr^{3+} 4f $\rightarrow$ 4f afterglow from the 254 nm UV-light charged LiScGeO$_4$:0.003Pr^{3+}. A near white QR code appears in the dark in Fig. 8(c3) as a result of the RT thermally stimulated 4f $\rightarrow$ 4f emissions of both Tb^{3+} and Pr^{3+} in LiLuGeO$_4$:0.005Tb^{3+},0.001Eu^{3+} and LiScGeO$_4$:0.003Pr^{3+}. Color-tailorable afterglow QR codes in Figs. 8(a3), 8(b3), and 8(c3) can be scanned by a mobile phone to readout the hidden information as illustrated in Fig. 8(c4) in the dark.

The prepared LiSc$_{0.25}$Lu$_{0.75}$GeO$_4$:0.005Tb^{3+},0.001Eu^{3+} solid solution was sifted by a 300 mesh screen. It was then dispersed in a silicone gel solution to make a square film with a size of ~5 × 5 cm^2 as shown in Fig. 9(a). Figures 9(b)–9(d) show that this film is both transparent and flexible. Figure 9(e) illustrates how the produced x-ray storage film can be utilized for x-ray imaging. The film was placed underneath an object and perpendicularly exposed to x-ray irradiation. After x-ray exposure, the object was removed and the film was kept at ~410 K in the dark to obtain an x-ray imaging owing to the thermally stimulated Tb^{3+} $^5D_4 \rightarrow$ ^7F_j emissions from LiSc$_{0.25}$Lu$_{0.75}$GeO$_4$:0.005Tb^{3+},0.001Eu^{3+} in the film as shown in Fig. 9(f). Figures 9(g) and 9(h) show that x-ray imaging with a high resolution of ~20 lp/mm can be realized by using this film.

To explore more advanced x-ray imaging, the LiSc$_{0.25}$Lu$_{0.75}$GeO$_4$:0.005Bi^{3+},0.001Eu^{3+} was dispersed into silicone gel to make a flexible film as shown in Fig. 9(i1). It was placed underneath two pens, which were perpendicularly exposed to x-rays in the dark as illustrated in Fig. 9(i2). The two pens were removed from the film after being irradiated by x-rays. The film was then heated to about 353 and 403 K to get two x-ray imaging photographs in Figs. 9(i3) and 9(i4). One then can clearly see the inner structures of the two pens. Note that the image color at the film center changes from purplish red to blue with increasing temperature. This is because of the increased ratio of the emission of Bi^{3+} $^3P_1 \rightarrow$ $^1S_0$ to that of Eu^{3+} 4f $\rightarrow$ 4f with increasing temperature. This temperature dependent image color property can be used as an encryption feature for developing advanced anti-counterfeiting application.

Figures 9(j1) and 9(j2) illustrate that the film can be bent to be placed underneath a flexible chip. They were then vortically exposed to x-rays. Red and blue x-ray imaging photographs appear at ~353 and ~403 K in Figs. 9(j3) and 9(j4) in the dark, respectively. It means that the film has potential use in x-ray imaging for curved objects.

III. DISCUSSION

A. Vacuum referred binding energy (VRBE) diagrams for LiLnGeO$_4$ (Ln = Sc or Lu)

Various luminescence phenomena like thermally stimulated afterglow and non-real-time force recording are associated with how electrons and holes are produced, transported, stored, or recombined during and after different types of excitations. The energy level locations of various defects, conduction band, and valence band are crucial to unravel the luminescence and charge carrier storage mechanisms. Based on a systematic spectroscopy and thermoluminescence study, the vacuum referred binding energy (VRBE) diagrams for LiLnGeO$_4$ (Ln = Sc or Lu) will first be constructed. They are then exploited to explain luminescence phenomena and to develop smart storage phosphors for various applications.

Monitored at typical Eu^{3+} emission at 612 nm, an excitation band peaked at ~223 nm appears in the PLE spectrum of LiScGeO$_4$:0.01Eu^{3+} in Fig. 2(b). A similar band also emerges in LiScGeO$_4$:0.005Eu^{3+} at 10 K in Fig. 2(c) and in LiSc$_{0.25}$Lu$_{0.75}$GeO$_4$:0.005Eu^{3+} at 10 K in Fig. S7(b). The excitation band is then attributed to the charge transfer (CT) from the valence band to Eu^{3+}, i.e., O$^{2-} \rightarrow$ Eu^{3+} CT.[29] An excitation band peaked at ~190.5 nm appears in the PLE spectrum ($\lambda_{em} = 501$ nm) of undoped LiScGeO$_4$ in Fig. 2(a). It is also observed in LiScGeO$_4$:0.005Pr^{3+} at 10 K in Fig. 2(e) and in LiScGeO$_4$:0.005Tb^{3+} at 10 K in Fig. 2(f). A similar and common excitation band peaked at ~197 nm appears in the PLE spectra of the undoped LiSc$_{0.25}$Lu$_{0.75}$GeO$_4$ in Fig. S7(a) and in Pr^{3+} or Tb^{3+} doped LiSc$_{0.25}$Lu$_{0.75}$GeO$_4$ at 10 K in Figs. S7(f) and S7(g). Upon excitation at ~190 or ~197 nm, a broad band emission feature appears in the undoped, Tb^{3+}, or Pr^{3+} single doped LiScGeO$_4$ in Figs. 2(a), 2(e), and 2(f) and in LiSc$_{0.25}$Lu$_{0.75}$GeO$_4$ compounds at 10 K in Figs. S7(a), S7(f), and S7(g). This verifies the nature of exciton emission. The common excitation band peaked at ~190.5 nm (6.50 eV) or ~197 nm (6.30 eV) is therefore assigned to the host exciton creation (E^{ex}) for LiScGeO$_4$ or LiSc$_{0.25}$Lu$_{0.75}$GeO$_4$, respectively. An excitation band located near 169 nm is observed in the PLE spectrum ($\lambda_{em} = 355$ or 385 nm) of LiScGeO$_4$:0.005Bi^{3+} at 10 K in Fig. 2(d). A similar excitation band peaked near 170 nm also appears in LiScGeO$_4$:0.005Tb^{3+} in Fig. 2(f), LiSc$_{0.25}$Lu$_{0.75}$GeO$_4$:0.005Bi^{3+} in Fig. S7(c), and LiSc$_{0.25}$Lu$_{0.75}$GeO$_4$: 0.005Tb^{3+} at 10 K in Fig. S7(g). The origin of these excitation bands is unclear.

To further confirm the VRBE diagram, the electron transfer from the Tb^{3+} or Pr^{3+} 4f ground states to the conduction band (CB) bottom has been studied. Generally, it is known as an intervalence charge transfer process.[30] This type of charge transfer can be observed in materials when the energy level of the CB bottom is below that of the lowest 5d states of Tb^{3+} and Pr^{3+}, for instance, in LiTaO$_3$, NaLuGeO$_4$, CdGeO$_3$,[31] BaWO$_4$,[32] and GdVO$_4$.[33] Once the energy level location of the conduction band bottom is known, one can deduce the energy level locations of Tb^{3+} and Pr^{3+} 4f ground states with respect to the CB by using the IVCT energies and vice versa. Since electrons are transferred from the Tb^{3+} and Pr^{3+} 4f ground states to the conduction band bottom and thereafter can be captured by traps, storage phosphor charging via the Tb^{3+} or Pr^{3+} IVCT excitation is then expected. Figures 2(e) and 2(f) show the PLE spectra of LiScGeO$_4$:0.005Pr^{3+} and LiScGeO$_4$:0.005Tb^{3+} measured at 10 K. The excitation bands peaked at 259 nm in Fig. 2(e) and at 250 nm in Fig. 2(f) are relatively broad. Figures 3(h) and 3(i) further demonstrate that traps can be filled by the excitation into these two bands.

The strongest excitation bands of Tb^{3+} are always from the spin allowed 4f $\rightarrow$ 5d transitions. For silicate and germanate compounds, each spin allowed band is accompanied by a much weaker spin forbidden transition at ~0.8 eV lower energy. This all suggests that the weak excitation band peaked at 300 nm (4.13 eV) in Fig. 2(f) is the first spin forbidden transition to the lowest crystal field split 5d state. The first spin allowed band is then expected at about 0.8 eV higher energy or around 252 nm. Therefore, we assign the 250 nm (4.96 eV) band to the first spin allowed transition. The higher energy excitation band peaked near 232 nm (5.34 eV) is then most likely the second spin allowed 4f $\rightarrow$ 5d band that should be accompanied by the second spin forbidden transition at 0.83 eV lower energy or 4.51 eV (275 nm). This is probably too weak to appear in Fig. 2(f). The band peaked at 268.5 nm (4.62 eV) is then most likely the Tb$^{3+} \rightarrow$ CB IVCT band with intensity

in between that of the first spin allowed and first spin forbidden 4f → 5d bands. This assignment is analogous to the one made for NaLuGeO$_4$:0.005Tb^{3+} in Fig. 4(d) in Ref. 34.

We next inspect the excitation bands peaked at 240 nm (5.17 eV) and 259 nm (4.79 eV) for LiScGeO$_4$:0.005Pr^{3+} in Fig. 2(e). On average, the first 4f → 5d transition in Pr^{3+} is at ~0.13 eV lower energy than in Tb^{3+}. With the assignments for Tb^{3+} above, one then expects that the first and second 4f → 5d transitions for Pr^{3+} are at ~4.83 eV (257 nm) and ~5.21 eV (238 nm), respectively. This then suggests that the excitation band peaked at ~259 nm (4.79 eV) is the first 4f → 5d transition and the excitation band peaked at ~240 nm (5.17 eV) is the second 4f → 5d transition. The Pr^{3+}→CB IVCT band is expected at similar energy as for Tb^{3+} → CB IVCT band (4.62 eV), which is then hidden under the more intense 4f → 5d bands of Pr^{3+}. Unfortunately, the 4f → 5d and IVCT band energies are quite close and one should therefore regard the assignments as tentative. The ionic radii of Li$^+$ (CN = 6), Sc^{3+} (CN = 6), Tb^{3+} (CN = 6), Pr^{3+} (CN = 6), Eu^{3+} (CN = 6), Bi^{3+} (CN = 6), and Ge^{4+} (CN = 4) are 0.76, 0.75, 0.92, 0.99, 0.95, 1.03, and 0.39 Å, respectively. Another complicating factor is the almost similar ionic radius of Li$^+$ and Sc^{3+} that creates various possible defect structures. Tb^{3+} often occupies a Sc^{3+} site but may also occupy a Li$^+$ site, which is then charge compensated by Li$^+$ on a nearby Sc^{3+} site (so-called anti-site occupation). The same applies to Pr^{3+}, Eu^{3+}, and Bi^{3+}.

With the estimated U parameters of 6.90 and 6.94 eV, and the above determined transition energies for host exciton creation (E^{ex}), O^{2-} → Eu^{3+} CT (E^{CT}), and IVCT from Tb^{3+} or Pr^{3+} to the CB bottom, the VRBE diagrams of LiScGeO$_4$ and LiSc$_{0.25}$Lu$_{0.75}$GeO$_4$ with the energy level locations of various divalent and trivalent lanthanide lanthanides were constructed as shown in Fig. 1 and S1. For comparison, the revised VRBE diagram for LiLuGeO$_4$ is shown in Fig. S2 by utilizing improved VRBE parameters in Ref. 21. Although it differs only a few 0.1 eV from that of LiScGeO$_4$, it is still of relevance for the location of TL glow peaks.

B. VRBE at Bi^{3+} $^1S_0$ and Bi^{2+} $^2P_{1/2}$ in LiScGeO$_4$ and LiSc$_{0.25}$Lu$_{0.75}$GeO$_4$

Figure 2(d) shows the photoluminescence excitation spectrum of LiScGeO$_4$:0.005Bi^{3+} at 10 K. In Ref. 35, the following empirical relation between the energy of the Bi^{3+} $^1S_0$ → $^3P_1$ (A-band) transition (E$_A$) and the $^1S_0$ → $^1P_1$ transition (E$_{BiC}$) was established as follows:

$$E_{BiC} = 3.236 + 2.290 \times (E_A - 2.972)^{0.856}. \qquad (2)$$

Using Eq. (2) and the Bi^{3+} $^1S_0$ → $^3P_1$ transition (E$_A$) at 297.6 and 308 nm for LiScGeO$_4$:0.005Bi^{3+}, the Bi^{3+} $^1S_0$ → $^1P_1$ (E$_{BiC}$) is to be expected near 5.90 eV (210 nm) and 5.63 eV (220 nm). The same applies to LiSc$_{0.25}$Lu$_{0.75}$GeO$_4$:0.005Bi^{3+} at 10 K in Fig. S7(c). The experimentally detected high energy excitation bands peaked near 197 nm in Fig. 2(d) and near 202 nm in Fig. S7(c) are close to the above predicted Bi^{3+} $^1S_0$ → $^1P_1$ transition energy values. They are then ascribed to the Bi^{3+} $^1S_0$ → $^1P_1$ transition, i.e., Bi^{3+} C-band.[36] The slightly lower energy but broader excitation band peaked at ~231.9 nm in Figs. 2(d) and S7(c) is then assigned to the electron transfer from the Bi^{3+} $^1S_0$ ground state to the conduction band bottom, i.e., the Bi^{3+} D-band.[22,37] Generally, traps in persistent luminescence or storage phosphors can be filled by the Bi^{3+} D-band

excitation. This feature is consistent with the thermoluminescence excitation plot of LiScGeO$_4$:0.003Bi^{3+} in Fig. 3(g).

Subtracting the energy values of Bi^{3+} D-bands from the conduction band bottom (E$_c$) energies, the VRBEs in the Bi^{3+} $^1S_0$ ground states are found to be −8.11 eV for LiScGeO$_4$, −8.34 eV for LiSc$_{0.25}$Lu$_{0.75}$GeO$_4$, and −8.06 eV for LiLuGeO$_4$. They are in agreement with the result in Ref. 38 that the VRBE in the Bi^{3+} $^1S_0$ ground state appears near −8 eV for compounds with a U-value near 7.0 eV as in LiScGeO$_4$. The VRBEs in the Bi^{3+} $^3P_1$ and $^1P_1$ excited states can then be determined by adding the Bi^{3+} A-band and C-band energies to the VRBEs in the Bi^{3+} $^1S_0$ ground states. The VRBE in the $^2P_{1/2}$ ground state of Bi^{2+} was found in the range from −3 to −4 eV in different oxide compounds.[39] It is assumed that the same range applies to LiScGeO$_4$, LiSc$_{0.25}$Lu$_{0.75}$GeO$_4$, and LiLuGeO$_4$ in this work. All the obtained Bi^{3+} and Bi^{2+} energy level locations are drawn in the VRBE diagrams as shown in Figs. 1, S1, and S2.

C. Rational design of storage phosphors by combining VRBE diagrams with conduction band engineering

The VRBE diagram of LiScGeO$_4$ in Fig. 1 predicts that Eu^{3+} acts as an ~1.25 eV deep electron trapping center, while the Pr^{3+}, Tb^{3+}, and Bi^{3+} act as about 2.15, 2.19, and 1.5 eV deep hole capturing centers, respectively. The similar applies to LiLuGeO$_4$ in Fig. S2. Figures 3(a)–3(f) evidence that Pr^{3+}, Tb^{3+}, and Bi^{3+} indeed work as recombination and luminescence centers in LiScGeO$_4$. Combining a less deep Eu^{3+} electron trap with deep Pr^{3+}, Tb^{3+}, and Bi^{3+} hole traps, it is expected that the electrons stored at Eu^{2+} will liberate at lower temperature than the hole captured at Pr^{4+}, Tb^{4+}, or Bi^{4+} in LiScGeO$_4$. Figure 4(a) shows that a new and common TL glow band peaked at ~461 K corresponding with a trapping depth of ~1.07 eV indeed appears in the Eu^{3+} co-doped LiScGeO$_4$. The similar applies to Eu^{3+} co-doped LiLuGeO$_4$ in Fig. 4(c) where a new and common TL band peaked at about 417 K corresponding with a trapping depth of ~0.98 eV also emerges. We therefore attribute the new and common TL glow band peaked at ~461 K for LiScGeO$_4$ and at ~417 K for LiLuGeO$_4$ to the electron release from Eu^{2+} that recombines with the holes located at Bi^{4+}, Pr^{4+}, or Tb^{4+}. The energy released by recombination excites Bi^{3+}, Pr^{3+}, and Tb^{3+} to their excited states and then Bi^{3+} A-band, Pr^{3+}, and Tb^{3+} characteristic 4f → 4f emissions are observed during TL-readout.

The VRBE diagrams of LiScGeO$_4$, LiSc$_{0.25}$Lu$_{0.75}$GeO$_4$, and LiLuGeO$_4$ in Figs. 1, S1, and S2 predict that the VRBE at the conduction band bottom slightly decreases by ~0.1 eV when the Sc is replaced by Lu. Such a small difference is smaller than the accuracy of the VRBE diagrams. Figure 4(b) and S10 demonstrate that the Eu^{2+} TL glow peak shifts to 40–60 K lower temperature in LiSc$_{1-x}$Lu$_x$GeO$_4$: 0.01Bi^{3+},0.001Eu^{3+}, LiSc$_{1-x}$Lu$_x$GeO$_4$:0.001Bi^{3+},0.001Eu^{3+}, and LiSc$_{1-x}$Lu$_x$GeO$_4$:0.005Tb^{3+},0.001Eu^{3+} when the x is increased from 0 to 1. This experimentally evidence that the Eu^{3+} trapping depth is slightly decreased by 0.1 eV, which can be useful to verify the prediction of the small Eu^{3+} trap depth variation from the VRBE diagrams in Figs. 1, S1, and S2. We therefore ascribe the TL band shifting toward 40–60 K lower temperature to the decreased activation energy for electron liberation from Eu^{2+} due to the conduction band lowering with increasing x in LiSc$_{1-x}$Lu$_x$GeO$_4$.

D. Evaluating non-real-time force recording application

Figure 7(c) compares the TL glow curves of LiSc$_{0.25}$Lu$_{0.75}$GeO$_4$: 0.005Tb^{3+},0.001Eu^{3+} solid solution charged by grinding, 254 nm UV-light, or x-rays. A new wide TL band peaked at ~656 K in the temperature range from ~525 to 723 K appears only when the compound was mechanically ground in an agate mortar with a pestle. It indicates that new traps were formed by mechanical grinding, which can be filled with a part of the free charge carriers yielded by means of mechanical excitations. The similar applies to other mechanically ground LiSc$_{1-x}$Lu$_x$GeO$_4$ compounds in Fig. 7(a) and S23–S25 where new and wide TL bands repeatedly appear in the temperature range from about 500 to 723 K. These new TL bands are well above RT. It means that charge carriers formed by mechanical stimulation can be stably stored at RT. The amount of the stored charge carriers linearly increases with increasing the grinding force duration as evidenced in Figs. 7(b), S24, and S25(e). These results collectively imply that the developed Eu^{3+} co-doped LiSc$_{1-x}$Lu$_x$GeO$_4$ compounds have potential utilization for the non-real-time force recording application as illustrated in Fig. 7(e).

The trapping depths of these new TL bands have been roughly determined to be in the range from 1.4 to 1.6 eV by utilizing Eq. (1), T$_m$ values, and the frequency factors obtained in Fig. 4(e). Using these calculated trapping depths, the VRBEs in the energy level locations of these traps are placed between −4.1 and −4.3 eV. They have been collectively labeled as traps FS in Fig. 1. During mechanical stimulation with grinding, free charge carriers can be generated in the LiSc$_{1-x}$Lu$_x$GeO$_4$ compounds, possibly with a triboelectricity[9,40] or piezoelectricity[41] excitation route. The produced electrons move freely through the conduction band and then be captured at traps FS. The produced holes move freely in the valence band, which can be finally trapped by Tb^{3+} or Bi^{3+}, forming Tb^{4+} or Bi^{4+}. Figure 7(c) shows the TL glow curves of LiSc$_{0.25}$Lu$_{0.75}$GeO$_4$:0.005Tb^{3+},0.001Eu^{3+} charged first by grinding for 300 s and then stimulated by 365 nm UV-light for different durations from 0 to 300 s. The energy of 365 nm (3.40 eV) UV-light is higher than the above calculated trapping depths. During exposure to 365 nm UV-light or thermal stimulation during TL-readout, the stored charge carriers formed by mechanical stimulation can be excited to recombine and yield luminescence.

E. Evaluating anti-counterfeiting and x-ray imaging applications

Figures 5(d), 5(e), S21, and S22 show the TL glow curves of Eu^{3+} co-doped LiSc$_{1-x}$Lu$_x$GeO$_4$ irradiated first by 254 nm UV-light and then with additional photon stimulation. The energies of the used wide range 365 nm (~3.4 eV) UV-light to 850 nm light (~1.5 eV) are higher than that of the Eu^{3+} trapping depth (~1 eV) as verified in Fig. 4(e). It means that the electrons trapped at Eu^{2+} can be excited to the conduction band with such photon stimulation. The excited electrons then relax to the conduction band bottom and move to recombine with the holes stored at Bi^{4+} or Tb^{4+}, forming optically stimulated Bi^{3+} ^{3}P$_1$ → ^{1}S$_0$ or Tb^{3+} ^{5}D$_4$ → ^{7}F$_j$ emissions like in Fig. 5(f).

Figures 5(a) and S19 evidence that the amount of stored charge carriers at Eu^{2+} linearly increases with increasing the x-ray exposure duration. Figures 5(b) and 5(c) evidence that the amount of stored charge carriers at Eu^{2+} has a low fading rate. Figure 5(d)–5(f) evidence that the stored charge carriers at Eu^{2+} can be released by means of

efficiently optical stimulated luminescence with a wide range 365–850 nm infrared light. Figures 6(a) and 6(d) evidence that the optimized LiSc$_{0.25}$Lu$_{0.75}$GeO$_4$:0.001Bi^{3+},0.001Eu^{3+} has excellent charge carrier storage capacity and chemical stability. The emission wavelength can be tailored from ultraviolet A (UVA) to red by selecting different hole trapping and luminescence centers of Bi^{3+}, Tb^{3+}, or Pr^{3+} as demonstrated in Figs. 3(a)–3(f). These features collectively indicate that the developed Eu^{3+} co-doped LiSc$_{1-x}$Lu$_x$GeO$_4$ storage phosphors have potential use as smart light dosimeters for anti-counterfeiting and x-ray imaging applications as illustrated in Figs. 8 and 9.

IV. CONCLUSIONS

In this work, data from photoluminescence spectroscopy and thermoluminescence studies have been used to establish the vacuum referred binding energy (VRBE) diagrams for LiScGeO$_4$, LiSc$_{0.25}$Lu$_{0.75}$GeO$_4$, and LiLuGeO$_4$ family of compounds. The photoluminescence emission and excitation spectra of undoped, Bi^{3+}, Eu^{3+}, Tb^{3+}, or Pr^{3+} single doped LiScGeO$_4$ and LiSc$_{0.25}$Lu$_{0.75}$GeO$_4$ were first studied at 10 K or RT in the spectral range from 125 to 750 nm. The results were then utilized to establish the VRBE diagrams for the LiSc$_{1-x}$Lu$_x$GeO$_4$ family of compounds, which provide the VRBEs in the ground and excited states of Bi^{3+}, trivalent, and divalent lanthanides. The VRBEs in the Bi^{3+} ^{1}S$_0$ ground states are about −8.11 eV for LiScGeO$_4$, −8.34 eV for LiSc$_{0.25}$Lu$_{0.75}$GeO$_4$, and −8.06 eV for LiLuGeO$_4$. The VRBEs in the Bi^{2+} ^{2}P$_1$ ground states were assumed around −3.5 ± 0.5 eV, which need to be verified further. These obtained VRBE diagrams are helpful to understand the trapping and de-trapping processes of charge carriers with various physical excitations, which then can guide us to rationally exploit storage phosphors for various applications.

As an example, the Bi^{3+} or/and Ln^{3+} (Ln = Tb, Pr, or Eu) doped LiSc$_{1-x}$Lu$_x$GeO$_4$ family of compounds were systematically investigated. By combining Eu^{3+} with Bi^{3+}, Tb^{3+}, or Pr^{3+}, Eu^{3+} works as an ~1.0 eV deep electron capturing center, while Bi^{3+}, Tb^{3+}, or Pr^{3+} work as about 1.5, 2.15, or 2.19 eV deep hole capturing and recombination centers in LiScGeO$_4$. A common Eu^{2+} TL glow band peaked near 461 K appears in x-ray irradiated LiScGeO$_4$ at $\beta = 1$ K/s. During TL-readout, the electrons stored at Eu^{2+} are released to combine with the holes stored at Bi^{4+}, Tb^{4+}, or Pr^{4+}, yielding characteristic Bi^{3+} ^{3}P$_1$ → ^{1}S$_0$, Tb^{3+}, or Pr^{3+} 4f → 4f transitions. The Eu^{3+} electron trapping depth can be controlled by tailoring x in LiSc$_{1-x}$Lu$_x$GeO$_4$: 0.001Bi^{3+},0.001Eu^{3+} and LiSc$_{1-x}$Lu$_x$GeO$_4$:0.005Tb^{3+},0.001Eu^{3+}, resulting in conduction band engineering. The integrated TL intensity of the optimized LiSc$_{0.25}$Lu$_{0.75}$GeO$_4$:0.001Bi^{3+},0.001Eu^{3+} irradiated by x-rays is about two times higher than that of the state-of-the-art x-ray storage phosphor BaFBr(I):Eu^{2+}. Particularly, a force induced charge carrier storage phenomenon appears in Eu^{3+} co-doped LiSc$_{1-x}$Lu$_x$GeO$_4$ (x = 0–1) compounds. The amount of stored charge carriers by mechanical excitation linearly increases with increasing the grinding duration. During grinding excitation, 254 nm UV-light, or x-ray charging, free charge carriers are first stored at Eu^{2+} or unintended defects, which then can be liberated by means of an optically stimulated luminescence process with a wide range 365–850 nm stimulation. Proof-of-concept non-real-time force recording, anti-counterfeiting, and x-ray imaging applications were proposed by utilizing the developed LiSc$_{1-x}$Lu$_x$GeO$_4$ storage phosphors. This work not only deepens our understanding of the capturing and de-trapping processes with various physical excitations but can also trigger scientists to

rationally discover new storage phosphors by constructing and exploiting the VRBEs in the energy level locations of bismuth and lanthanide levels in different compounds.

V. EXPERIMENTAL

We bought the Li_2CO_3 (99.99%) from the Macklin Biochemical Technology company (Shanghai, China). The other raw materials were bought from the Aladdin Biochemical Technology company (Shanghai, China). All the starting chemicals were stored in a dry cabinet and then utilized without further treatment. Bi^{3+} and/or lanthanides doped $LiScGeO_4$, $LiLuGeO_4$, or $LiSc_{1-x}Lu_xGeO_4$ solid solutions were synthesized by using a high temperature solid-state reaction method. An excess of 10% Li^+ above the compound composition stoichiometry has been used in order to compensate the loss of Li^+ during synthesis at high temperature. The masses of dopants were calculated based on molar ratios between different elements in compound compositions like in $LiSc_{0.25}Lu_{0.75}GeO_4:0.001Bi^{3+},0.001Eu^{3+}$. About 0.8 g stoichiometric mixture was composed of Li_2CO_3 (99.99%), Sc_2O_3 (99.99%), Lu_2O_3 (99.99%), GeO_2 (99.99%), Bi_2O_3 (99.99%), Eu_2O_3 (99.99%), Pr_6O_{11} (99.99%), or Tb_4O_7 (99.99%). The mixture was placed in an agate mortar and then carefully mixed with the help of a pestle and acetone solution in a fume hood. The homogeneously mixed powder was placed in a covered corundum crucible. It was first kept at $800\,°C$ for 2 h and then at $1150\,°C$ for 6 h or 10 h under ambient atmosphere in a tube furnace. A heating rate of $3\,°C/min$ was employed for the furnace. Finally, the synthesized compounds were naturally cooled down to room temperature (RT, $\sim$298 K) and then were ground prior to further measurements or treatment.

The structures of all the synthesized compounds were checked with a Japan Rigaku SmartLa x-ray diffraction setup. Photoluminescence emission (PL) and excitation (PLE) spectra in the spectral range from $\sim$130 to $\sim$750 nm were recorded in vacuum at 10 K by using the Beijing VUV spectroscopy station BSRF facility. The above 200 nm PLE, PL, thermoluminescence (TL) excitation (TLE), room temperature (RT) isothermal afterglow, and x-ray excited emission spectra were measured by utilizing an Edinburgh FLS980 fluorescence spectrometer. It contains a MOXTEK TUB00154-9I-W06 x-ray tube (60 KV, 200 μA, 12 W), a 450 W xenon lamp, a 4 W Hg lamp, and a Hamamatsu R928P photomultiplier. The emission spectra were corrected by the wavelength dependent quantum efficiencies of the used R928P photomultiplier. All the obtained photoluminescence excitation spectra have been corrected by the excitation intensities as a function of wavelength. Thermoluminescence (TL), x-ray excited emission intensities as a function of time, and RT isothermal decay curves were recorded with a facility. It contains a MOXTEK TUB00083-2 x-ray tube, a 4 W Hg lamp, a red-sensitive Hamamatsu R928P photomultiplier, a heater operated in the temperature range from 300 to $\sim$773 K, a cryostat operated in the temperature range from 100 to 600 K, and an ultraviolet to infrared spectrometer (Ocean Optics, QE65000), and a SCHOTT BG-39 filter. For TL measurements, a constant sample mass of $\sim$0.0300 g was used. For a fair TL intensity comparison, a fixed dose of x-rays from the MOXTEK TUB00083-2 x-ray tube operated at 30 KV, 50 μA, 1.5 W was utilized. The x-ray dose rate is about 0.5 Gy/min. A fixed dose ($\sim$300 μW/cm^2) of 254 nm UV-light from a 4 W Hg lamp was used. The TL intensities were corrected by the sample mass and the x-ray or 254 nm UV-light charging time. The commercial reference x-ray storage phosphor $BaFBr(I):Eu^{2+}$ was purchased from the Agfa-Gevaert company.[5] The state-of-the-art $Al_2O_3:C$ chip with 0.5 cm diameter and 1 mm thick was bought from the

LANDAUER company. The commercial $ZnS:Mn^{2+}$ mechanoluminescence material has been bought from the Shanghai Keyan phosphor technology company (https://kpt.net.cn/en/contact_en/).

To explore x-ray imaging and color-tailorable afterglow for anticounterfeiting applications, the synthesized powder storage phosphors were carefully sifted by a 200 mesh screen. The sifted $LiLuGeO_4:$ $0.005Tb^{3+},0.001Eu^{3+}$ and/or $LiScGeO_4:0.003Pr^{3+}$ compounds were dispersed in a transparent ink solution to print a QR code or a photograph of Albert Einstein on a sheet of paper by using a typical screen printing technique. The $LiSc_{0.25}Lu_{0.75}GeO_4:0.005Tb^{3+},0.001Eu^{3+}$ x-ray storage phosphor was first well mixed with silicone gel solution (Sylgard 184, Dow Corning). The mixture was then placed in a smooth sapphire plate based mold, which was kept at $75\,°C$ with a duration of 3 h. A nice Nikon D850 camera or an iPhone 6s Plus was utilized to take the photographs shown in this work.

SUPPLEMENTARY MATERIAL

See the supplementary material for details on VRBE diagrams, XRD patterns, photoluminescence excitation (PLE) spectra, emission (PL) spectra, afterglow decay curves, thermoluminescence (TL) glow curves, and afterglow movies of the $LiSc_{1-x}Lu_xGeO_4$ family of compounds.

AUTHOR DECLARATIONS
Conflict of Interest

The authors have no conflicts to disclose.

Author Contributions

Tianshuai Lyu: Conceptualization (lead); Data curation (lead); Funding acquisition (lead); Investigation (lead); Writing – original draft (lead); Writing – review & editing (lead). **Pieter Dorenbos:** Formal analysis (supporting); Resources (supporting); Writing – review & editing (supporting).

DATA AVAILABILITY

The data that support the findings of this study are available from the corresponding author upon reasonable request.

REFERENCES

[1]D. Poelman, D. van der Heggen, J. Du, E. Cosaert, and P. F. Smet, J. Appl. Phys. **128**(24), 240903 (2020); F. Kang, G. Sun, P. Boutinaud, H. Wu, F.-X. Ma, J. Lu,

J. Gan, H. Bian, F. Gao, and S. Xiao, Chem. Eng. J. **403**, 126099 (2021); C. Liao, H. Wu, H. Wu, L. Zhang, G.-H. Pan, Z. Hao, F. Liu, X.-J. Wang, and J. Zhang, Laser Photonics Rev. **17**(8), 2300016 (2023); S. Hirata, Appl. Phys. Rev. **9**(1), 011304 (2022).

[2]L. Liang, J. Chen, K. Shao, X. Qin, Z. Pan, and X. Liu, Nat. Mater. **22**(3), 289 (2023); T. Shi, F. Chen, X. Zhao, J. Zhang, X.-J. Wang, and F. Liu, Appl. Phys. Lett. **121**(19), 191902 (2022); S. Lin, H. Lin, C. Ma, Y. Cheng, S. Ye, F. Lin, R. Li, J. Xu, and Y. Wang, Light: Sci. Appl. **9**(1), 22 (2020); E. Aboelezz and B. W. Pogue, Appl. Phys. Rev. **10**(2), 021312 (2023).

[3]Y. Zhuang, L. Wang, Y. Lv, T.-L. Zhou, and R.-J. Xie, Adv. Funct. Mater. **28**(8), 1705769 (2018); F. Xie, D. Chen, Y. Zhang, X. Lv, X. Chen, K. Sun, and Y. Liang, J. Mater. Chem. C **11**(47), 16772 (2023); Q. Peng, T. Wang, H. Tang, T. Ji, W. Wang, J. Xiao, X. Li, Z. Liu, J. Qiu, X. Yu, and X. Xu, Laser Photonics Rev. **16**(12), 2200449 (2022); S. Lin, H. Lin, G. Chen, B. Wang, X. Yue, Q. Huang, J. Xu, Y. Cheng, and Y. Wang, Laser Photonics Rev. **15**(7), 2100044 (2021); N. Gan, X. Zou, Y. Zhang, L. Gu, and Z. An, Appl. Phys. Rev. **10**(2), 021313 (2023).

[4]S. Lin, H. Lin, Q. Huang, Y. Cheng, J. Xu, J. Wang, X. Xiang, C. Wang, L. Zhang, and Y. Wang, Laser Photonics Rev. **13**(4), 1900006 (2019).

[5]A. Dobrowolska, A. J. J. Bos, and P. Dorenbos, Phys. Status Solidi RRL **13**(3), 1800502 (2019).

[6]P. I. C. Claro, E. P. B. S. Borges, G. R. Schleder, N. L. Archilha, A. Pinto, M. Carvalho, C. E. Driemeier, A. Fazzio, and R. F. Gouveia, Appl. Phys. Rev. **10**(2), 021302 (2023).

[7]P. Leblans, D. Vandenbroucke, and P. Willems, Materials **4**(6), 1034 (2011).

[8]Y. Zhuang and R.-J. Xie, Adv. Mater. **33**(50), 2005925 (2021); J.-C. G. Bünzli and K.-L. Wong, J. Rare Earths **36**(1), 1 (2018); A. Feng and P. F. Smet, Materials **11**(4), 484 (2018); T. Zheng, M. Runowski, I. R. Martín, K. Soler-Carracedo, L. Peng, M. Skwierczyńska, M. Sójka, J. Barzowska, S. Mahlik, H. Hemmerich, F. Rivera-López, P. Kulpiński, V. Lavín, D. Alonso, and D. Peng, Adv. Mater. **35**(40), 2304140 (2023); S. Liu, Y. Zheng, D. Peng, J. Zhao, Z. Song, and Q. Liu, Adv. Funct. Mater. **33**(3), 2209275 (2023); J. Xiao, Y. Cai, Y. Song, H. Tang, P. Zhang, Q. Peng, X. Xu, Z. Liu, and L. Zhao, Laser Photonics Rev. **2023**, 2301002.

[9]Z. Huang, B. Chen, B. Ren, D. Tu, Z. Wang, C. Wang, Y. Zheng, X. Li, D. Wang, Z. Ren, S. Qu, Z. Chen, C. Xu, Y. Fu, and D. Peng, Adv. Sci. **10**(3), 2204925 (2023).

[10]C. Chen, Y. Zhuang, X. Li, F. Lin, D. Peng, D. Tu, A. Xie, and R.-J. Xie, Adv. Funct. Mater. **31**(25), 2101567 (2021); S. Song, H.-S. Choi, C.-H. Cho, S. K. Lim, and S. M. Jeong, Appl. Phys. Rev. **9**(1), 011423 (2022).

[11]S. Zhou, Y. Cheng, J. Xu, H. Lin, W. Liang, and Y. Wang, Laser Photonics Rev. **16**(5), 2100666 (2022); X. Yang, Y. Cheng, J. Xu, H. Lin, and Y. Wang, Laser Photonics Rev. **16**(11), 2200365 (2022).

[12]M. Zhu, J. Luo, T. Liang, Y. Zheng, X. Li, Z. Huang, B. Ren, X. Zhang, J. Li, Z. Zheng, J. Wu, Y. Zhong, Y. Wang, C. Wang, and D. Peng, Laser Photonics Rev. **17**(12), 2300517 (2023); P. Zhang, W. Xie, Z. Lin, X. Huang, Y. Yang, and W. Liu, Laser Photonics Rev. **17**(12), 2300266 (2023).

[13]Y. Zhuang, X. Li, F. Lin, C. Chen, Z. Wu, H. Luo, L. Jin, and R.-J. Xie, Adv. Mater. **34**(36), 2202864 (2022).

[14]T. Lyu, P. Dorenbos, and Z. Wei, Laser Photonics Rev. **17**(11), 2300323 (2023).

[15]T. Lyu, P. Dorenbos, P. Xiong, and Z. Wei, Adv. Funct. Mater. **32**(39), 2206024 (2022).

[16]Y. Zhuang, D. Tu, C. Chen, L. Wang, H. Zhang, H. Xue, C. Yuan, G. Chen, C. Pan, L. Dai, and R.-J. Xie, Light: Sci. Appl. **9**(1), 182 (2020).

[17]T. Lyu and P. Dorenbos, J. Mater. Chem. C **6**(2), 369 (2018).

[18]T. Lyu, P. Dorenbos, and Z. Wei, Chem. Eng. J. **461**, 141685 (2023); T. Lyu, P. Dorenbos, C. Li, S. Li, J. Xu, and Z. Wei, Chem. Eng. J. **435**, 135038 (2022); T. Lyu and P. Dorenbos, Chem. Eng. J. **400**, 124776 (2020); T. Lyu and P. Dorenbos, Chem. Eng. J. **372**, 978 (2019).

[19]P. Dorenbos, J. Mater. Chem. **22**(42), 22344 (2012); Phys. Rev. B **85**(16), 165107 (2012); T. Lyu, Chin. J. Lumin. **43**(9), 1413 (2022).

[20]J. Xu and S. Tanabe, J. Lumin. **205**, 581 (2019).

[21]P. Dorenbos, J. Lumin. **222**, 117164 (2020).

[22]T. Lyu and P. Dorenbos, J. Mater. Chem. C **6**(23), 6240 (2018).

[23]T. Lyu, P. Dorenbos, C. Li, and Z. Wei, Laser Photonics Rev. **16**(9), 2200055 (2022); T. Lyu and P. Dorenbos, Laser Photonics Rev. **16**(10), 2200304 (2022).

[24]Z. Zhou, P. Xiong, H. Liu, and M. Peng, Inorg. Chem. **59**(17), 12920 (2020); Y. Zhang, D. Chen, W. Wang, S. Yan, J. Liu, and Y. Liang, Inorg. Chem. Front. **7**(17), 3063 (2020).

[25]P. Dorenbos, J. Lumin. **267**, 120358 (2024).

[26]H. Luo, A. J. J. Bos, A. Dobrowolska, and P. Dorenbos, Phys. Chem. Chem. Phys. **17**(23), 15419 (2015).

[27]W. Wang, Z. Sun, X. He, Y. Wei, Z. Zou, J. Zhang, Z. Wang, Z. Zhang, and Y. Wang, J. Mater. Chem. C **5**(17), 4310 (2017).

[28]D. Kulesza, A. J. J. Bos, and E. Zych, Acta Mater. **231**, 117852 (2022); H. Luo, A. J. J. Bos, and P. Dorenbos, J. Phys. Chem. C **121**(16), 8760 (2017); A. J. J. Bos, P. Dorenbos, A. Bessière, A. Lecointre, M. Bedu, M. Bettinelli, and F. Piccinelli, Radiat. Meas. **46**(12), 1410 (2011); F. You, A. J. J. Bos, Q. Shi, S. Huang, and P. Dorenbos, Phys. Rev. B **85**(11), 115101 (2012); J. Ueda, P. Dorenbos, A. J. J. Bos, K. Kuroishi, and S. Tanabe, J. Mater. Chem. C **3**(22), 5642 (2015).

[29]P. Dorenbos, J. Lumin. **111**(1), 89 (2005); J. Mater. Chem. C **11**(24), 8129 (2023).

[30]P. Dorenbos, Opt. Mater. **91**, 333 (2019); P. Dorenbos, Opt. Mater. **69**, 8 (2017).

[31]S. Zhang, Y. Hu, L. Chen, G. Ju, Z. Wang, and J. Lin, Opt. Mater. **47**, 203 (2015).

[32]J. Lin, Z. Zeng, Q. Ma, Q. Wang, and Y. Zhang, Energy **64**, 551 (2014).

[33]A. H. Krumpel, E. van der Kolk, E. Cavalli, P. Boutinaud, M. Bettinelli, and P. Dorenbos, J. Phys.: Condens. Matter **21**(11), 115503 (2009); P. Boutinaud, R. Mahiou, E. Cavalli, and M. Bettinelli, Chem. Phys. Lett. **418**(1), 185 (2006).

[34]T. Lyu and P. Dorenbos, Chem. Mater. **32**(3), 1192 (2020).

[35]L. Wang, Q. Sun, Q. Liu, and J. Shi, J. Solid State Chem. **191**, 142 (2012).

[36]R. H. P. Awater and P. Dorenbos, J. Phys. Chem. C **120**(28), 15114 (2016); P. Dorenbos, ECS J. Solid State Sci. Technol. **10**(8), 086002 (2021); Y. Wei, Z. Gao, X. Yun, H. Yang, Y. Liu, and G. Li, Chem. Mater. **32**(19), 8747 (2020).

[37]P. Boutinaud, Phys. Chem. Chem. Phys. **25**(16), 11027 (2023).

[38]R. H. P. Awater and P. Dorenbos, J. Lumin. **184**, 221 (2017).

[39]R. H. P. Awater and P. Dorenbos, J. Lumin. **188**, 487 (2017).

[40]J.-C. Zhang, X. Wang, G. Marriott, and C.-N. Xu, Prog. Mater. Sci. **103**, 678 (2019); Z. Ma, Y. Han, Y. Bai, B. Liu, and Z. Wang, Chem. Eng. J. **456**, 141122 (2023); Y. Bai, F. Wang, L. Zhang, D. Wang, Y. Liang, S. Yang, and Z. Wang, Nano Energy **96**, 107075 (2022).

[41]C. Wang, R. Ma, D. Peng, X. Liu, J. Li, B. Jin, A. Shan, Y. Fu, L. Dong, W. Gao, Z. L. Wang, and C. Pan, InfoMat **3**(11), 1272 (2021); D. Tu, C.-N. Xu, S. Kamimura, Y. Horibe, H. Oshiro, L. Zhang, Y. Ishii, K. Hyodo, G. Marriott, N. Ueno, and X.-G. Zheng, Adv. Mater. **32**(25), 1908083 (2020); S. Liu, R. Liu, X. Yang, J. Li, M. Sun, C.-N. Xu, B. Huang, Y. Liang, and D. Tu, Nano Energy **93**, 106799 (2022); D. Tu, C.-N. Xu, A. Yoshida, M. Fujihala, J. Hirotsu, and X.-G. Zheng, Adv. Mater. **29**(22), 1606914 (2017); C.-N. Xu, T. Watanabe, M. Akiyama, and X.-G. Zheng, Appl. Phys. Lett. **74**(17), 2414 (1999).

06 March 2024 10:41:49